Study of Highly Correlated Systems on *h*-BN/Cu(111) using Cryogenic Scanning Tunneling Microscopy and Atomic Force Microscopy

Abhishek Grewal
Matrikelnr.: 3194256

Supervisor: Dr. Markus Ternes
1st Examiner: Prof. Jörg Wrachtrup
2nd Examiner: Prof. Klaus Kern

University of Stuttgart
&
Max Planck Institute for Solid State Research

A thesis submitted in partial fulfillment of
the requirements for the degree of
Master of Science in Physics

October, 2017

Declaration

I hereby declare that except where specific reference is made to the work of others, the contents of this thesis are original and have not been submitted in whole or in part for consideration for any other degree or qualification in this, or any other university. This dissertation is my own work and contains nothing which is the outcome of work done in collaboration with others, except as specified in the text.

Abhishek Grewal
October 2017

Abstract

Of the many fascinating topics in condensed matter physics, this work aims to cover two subtopics in some detail: 1) Manifestations of Kondo effect using single magnetic atoms on decoupled metal substrates. 2) How local variations in electronic or mechanical properties of the decoupling layer affect these observations. In addition to these areas of research, there will also be a focus on the optimization of tip-sample approach mechanism. An ingenious method to determine the stiffness of monolayer, discussed in [40, 41], is used to get the first impression of elasticity of h-BN/Cu(111). Along with the electronic characterization, this approach sheds some light on the long-standing debate of *h*-BN/Cu(111) being free of any mechanical corrugation [51, 81]. The first measurements of Kondo effect of Co and CoH_x species, which exist because of hydrogen adsorption, on this particular substrate are presented with a preliminary analysis of the observations.

Keywords: cryogenic combined STM/AFM, capacitance-based tip-sample approach, Φ variation, short-range forces, correlated atomic spins, Kondo effect, *h*-BN/Cu(111)

Acknowledgements

First and foremost, I would like to thank Prof. Klaus Kern, for the opportunity to carry out my thesis work in his labs with the excellent group of people he had assembled.

Next, I want to thank my supervisor, Dr. Markus Ternes, for his guidance, his trust and the freedom he gave me in pursuing my ideas in the lab. Your scientific curiosity is contagious. I thank Matthias Muenks for his excellent introduction to STM/AFM. Moreover, our discussions on ethics, politics, and much more are something I have and would always look forward to. I was fortunate that Dr. Yuqi Wang joined our subgroup and got caught up in our enthusiasm with the possibilities our experiment offers.

I would also like to thank all the other members of the Nanoscale Science Department at MPI-FKF for all the guidance and fun outings. I really could not wish for a better set of colleagues.

Table of contents

List of figures

Introduction

Over the last decades, technological progress has made it possible to investigate and control the matter on an atomic level. Reason for growing interest in nanoscience, apart from the hope of further miniaturization of microelectronic devices, is also the prospect of understanding novel physical and chemical behavior occurring at nanometer (or lower) scale. The study of single atoms and molecules provides new insight into the processes on surfaces and gives a fundamental basis for fabrication of nanostructured materials with potential applications in molecular electronics [31, 49] or spintronics [37, 98].

With the invention of scanning tunneling microscope (STM) by Binnig and Rohrer [5–7], a new method appeared to deal with nanometer scale structures. STM is a powerful tool to investigate and control properties of single atoms and molecules, and their interaction with the environment. Measurements at low temperature allow combining the imaging capabilities of STM with spectroscopic analysis, manipulation and chemical modification, which gives insight into the phenomena not accessible to other techniques [45, 86].

The instrument used in this thesis, a sub-Kelvin combined STM/AFM with a superconducting magnet (up to 14 T) and a single atom evaporator [40, 97] combined with the high stability environment of the Precision Laboratory at MPI-FKF [60, 85], provides a unique toolkit which is indeed capable of pushing the frontiers of science at the nanoscale.

The high degree of clarity and control provided by single atomic or molecular species on flat, clean substrates enable one to perform quantum simulations and study physics therein [14, 38, 88]. Experiments using controlled manipulation of single magnetic atoms like Co, Ti, etc. have provided unprecedented insight into the atomic scale magnetism and understanding of correlation strength dependent effects like the Kondo effect [43, 68]. It had already been observed that supporting layer has a non-negligible influence on the properties of adsorbates [46, 67] which is of central importance when it comes to investigating the Kondo effect. *h*-BN/Cu(111), which is prophesied to be an atomically flat passivity layer with only an electronic corrugation could help deconvolve the effect of conduction electrons from the substrate and local strain or defects in the supporting decoupling layer [51, 81].

Structure of the thesis

The experimental techniques used during the thesis and their theoretical background will be described in Chapter 1. One of the tasks undertaken at the onset of this thesis was optimization of approach mechanism. Chapter 2 provides an insight into the physical aspect that allows for such an optimization. A protocol to implement such optimization is discussed in the context of scanning probe instruments where the sample holder dimensions vary slightly leading to change in background reference capacitance values. Next, the structural and electronic properties of *h*-BN/Cu(111) are investigated. In Chapter 3, the preparation parameters and procedure are discussed. FER and KPFM measurements provide information about local Φ variation. An analysis of such resonances at valley and rims of *h*-BN/Cu(111) is presented using modes of a circular potential well. Following the electronic characterization, vertical stiffness of the adlayer is measured. A preliminary analysis of the data indicates that the mechanical corrugation of the layer is not significant. Later on, the Kondo effect in measurements using Co on *h*-BN/Cu(111) is reported. These species show a variety of spectroscopy signatures which are discussed in the context of adsorption sites and chemical nature of the adsorbates in Chapter 5. A summary of the results is presented in Chapter 6.

Chapter 1

Theory and Experimental setup

This chapter will give an introduction to basic principles of STM and nc-AFM, the experimental methods used in this thesis. In the next section, an introduction to Scanning Tunneling Spectroscopy (STS) is presented in the context of point spectroscopy and dI/dV map measurements. The primary instrument is a home-built Joule Thompson refrigerated combined STM and AFM (aka subK STM). The last section gives a brief description of the experimental capabilities of this instrument.

1.1 Scanning Tunneling Microscopy

The essence of STM is based on the tunneling experiments from the early 1960s where a bias voltage, V_B, was applied to two electrodes separated by insulating oxide layer leading to a tunneling current, I_T. The tunneling current is dependent on the applied bias and is directly proportional to the electronic density of states of the two electrodes and depends exponentially on the gap between the two electrodes. Thus, tunneling current provides information about the electronic structure near the Fermi level of the electrodes material. In case of STM, the two electrodes are the conducting sample and the sharp metallic tip. The tip can be placed freely over the sample in x, y, and z-directions with picometer resolution keeping a vacuum barrier between the tip and the sample. In the regime where the gap is ~ few Å, the electrons can quantum mechanically tunnel through the barrier between the two electrodes

1.1.1 Scanning modes

To harness the power of STM, a raster scanning mechanism is used. The tip is moved back and forth over the surface while a computer program records the tunneling current. The image generated has tunneling current encoded as a pixel colormap and (x,y) position of the pixel represents (x,y) position on the sample.

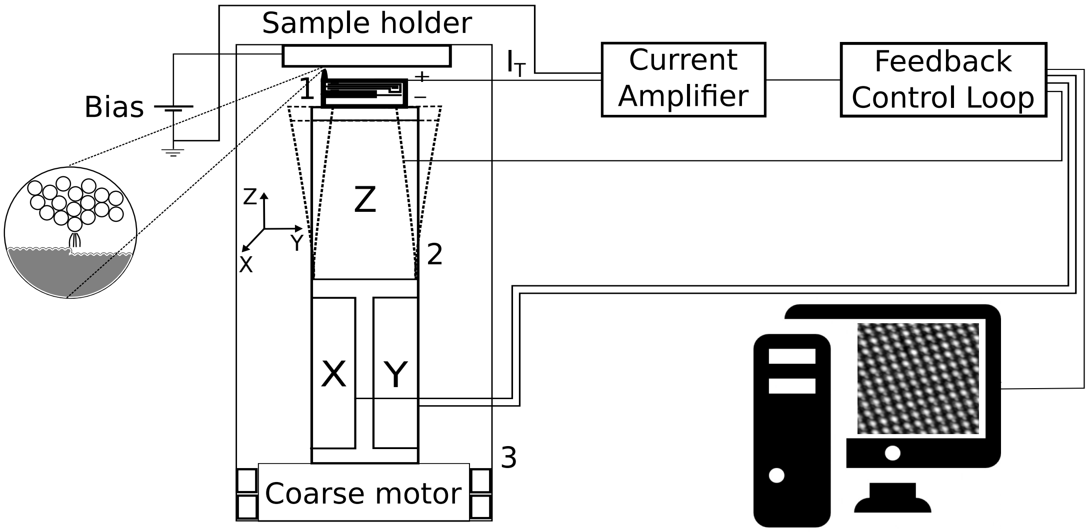

Fig. 1.1 Schematic of operating principle of a combined STM/AFM. 1. depicts the qPlus sensor fixed on the z-piezo housing the STM tip. 2. shows the z-piezo which is scanned using control electronics to scan the tip over the surface, and 3. shows the tip stage where the scanner sits.

The tip can be moved in two modes over the sample. The first, and the more common one being where a constant tunneling current is maintained between the tip and the sample by a feedback loop. In this mode, the image generation works the same except the pixel colormap encodes the tip height change instead of changes in the tunneling current. The other mode involves moving the tip at a constant height, which is riskier, as it can crash[1] into artifacts on the surface and going over steps might lead to severe loss of resolution. The images generated using the constant height mode are more accessible as the changes in tunneling current can be attributed to the local changes in surface and electronic structure. It gets more complicated to analyze the constant current mode data as the tip is being moved vertically to maintain constant tunneling current. Care needs to be taken to set feedback parameters in a way that the feedback loop can keep the constant current and thus, doesn't crash into artifacts on the surface. In case of a crash, or any other event which makes the tip dirty for that sake would require repreparation of the tip. This involves applying voltage pulses on the sample to force entities on the tip apex to drop to the surface or rearrange. Another way of tip cleansing is indenting it into the surface several nanometres until a clean tip is attained. This is verified by checking metal surface state by doing dI/dV measurement. To avoid this, the scanning speed used should be of the order of 10 $\mathrm{nm\,s^{-1}}$, more so for a combined STM/AFM. On the contrary, thermal drift in vertical height change must be of the order of 1% over the course of taking the image to use constant height mode safely. To be able to maintain a perfectly clean, stable tip being

---

[1] contact between the tip and sample which destroys the sanctity of the tip

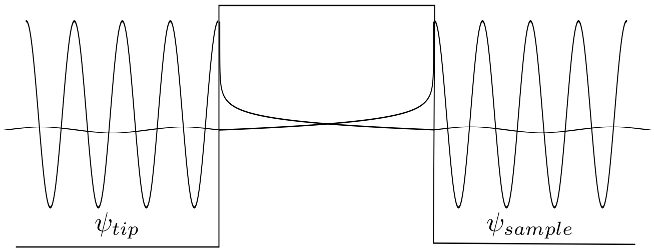

Fig. 1.2 In Bardeen approach, a time-dependent linear combination of exact solutions to the two one-electrode problems is used to construct and approximate wavefunction. Due to the decaying tails of ψ_{sample} and ψ_{tip}, the approximated wavefunction is not exact outside the barrier.

more critical than scan time, explains the constant current mode being more common.

1.1.2 Bardeen tunneling and Tersoff-Hamman approximation

The STM tunneling geometry inevitably being three dimensional requires a decent treatment than one-dimensional tunneling junction as neither wave-matching at boundaries nor Wentzel-Kramers-Brillouin approximation is straightforwardly expanded to three dimensions.

The tunneling problem can be viewed as a special case of a more general problem, current-voltage characteristics at an interface. The perturbative treatment considering weak tip-sample interaction circumvents to deal with the more complicated, latter problem. The Bardeen formalism for tunneling between two electrodes [2] forms the basis for most of the latest theories. Discussion by Alex D. Gottlieb and Lisa Wesoloski on the application of the theory to STM forms the basis of the discussion henceforth [33].

The idea is to separately treat tip and sample system across a square potential barrier as shown in Fig. 1.2. Simplest one-dimensional Schrödinger equation is solved with certain assumptions about electronic density of states. The electron transfer rate across the electrodes is calculated using Fermi's golden rule. Even though wavefunction for the two electrodes can be separately found it's arduous to take the effect of tip-sample interaction into account. But it's nothing to panic about as from general tunneling we know that wavefunction decay exponentially in the barrier region with decay constant of the order of 1 Å^{-1}. The tunneling gap in STM is a few Å [6], and thus there's minimal wavefunction overlap. The mathematical treatment of the above discussion can be found readily in literature but to discuss the subtle tunneling effects presented in later chapters it's essential to briefly go through it. Following assumptions are used in theoretical treatment:

1. Electron-electron interactions are ignored
2. Occupation of orthogonal states for both tip and sample are constant despite electron transfer going on between the two
3. Tip and sample are in electrochemical equilibrium
4. Tunneling effect is effect to justify treatment by first order perturbation theory

The single particle Hamiltonian that the particles must obey can be written as,

$$H\psi = -\frac{\hbar^2}{2m}\nabla^2\psi(\mathbf{r}) + V(\mathbf{r})\psi(\mathbf{r}) \tag{1.1}$$

Writing distinct Hamiltonian, as shown in Eq. 1.1, for tip and sample system to simplify solving of Schrödinger equation for the system,

$$\begin{aligned} H_{tip}\psi &= -\frac{\hbar^2}{2m}\nabla^2\psi(\mathbf{r}) + V_{tip}(\mathbf{r})\psi(\mathbf{r}) \\ H_{sample}\psi &= -\frac{\hbar^2}{2m}\nabla^2\psi(\mathbf{r}) + V_{sample}(\mathbf{r})\psi(\mathbf{r}) \end{aligned} \tag{1.2}$$

where V, for both tip and sample, is of the form,

$$V_{tip,sample} = \begin{cases} V(\mathbf{r}) & \text{if } \mathbf{r} \text{ in the tip or sample region} \\ 0 & \text{otherwise} \end{cases} \tag{1.3}$$

Assuming the electronic density of states for tip and sample to be $\rho_{tip}(E_n)$ and $\rho_{sample}(E_n)$, occupancy of which follow Fermi-Dirac statistics. Using Fermi's Golden rule [19] it can be shown that the rate of tunneling from an occupied sample state to an empty tip state is

$$\frac{2\pi}{\hbar}(1 - F_{\mu_{tip},T}(E))\rho_{tip}(E)M^2(\psi_{sample}) \tag{1.4}$$

where $F_{\mu_{tip},T}(E)$ is the occupancy of tip states at temperature T and μ_{tip} is the chemical potential. The square amplitude of scattering matrix element, M^2, connecting the tip and sample states is given by

$$M^2(\psi) = \frac{1}{N_E}\sum_{k:\ |E_k - E| < 2h/t} |\langle\phi_k|H - H_{sample}|\psi\rangle|^2 \tag{1.5}$$

where N_E is the number of tip states in the energy range $E - 2h/t$ to $E + 2h/t$. The prerequisite for tunneling to occur is the availability of electon density of states at the tip for electrons to scatter into. If we consider all the possibilites of electrons from occupied DOS to the unoccupied ones between the tip and sample. Summing over all the processes in play the tunneling current, I, can be written as

$$I = \frac{2\pi e}{\hbar} \sum_n \left\{ F_{\mu_{tip},T}(E_n)(1 - F_{\mu_{sample},T}(E_n)) - (1 - F_{\mu_{tip},T}(E_n))F_{\mu_{sample},T}(E_n) \right\} \rho_{tip}(E_n) M^2(\psi_n) \tag{1.6}$$

At T = 0 K the Fermi-Dirac function is reduced to a Heaviside function. Approximating the summation to an integral in Eq. 1.6, the tunneling current is written as

$$I = \pm\frac{2\pi e}{\hbar} \int_{\mu_{tip}}^{\mu_{sample}} \rho_{tip}(E) T(E) \rho_{sample}(E) dE \tag{1.7}$$

where $T(E)$ is mean $M^2(\psi_n)$ over all sample states lying in a small energy interval around E. The sign of I depends on relative chemical potential of the tip and sample.

Using low bias and low temperature conditions for tunneling for which $\rho_{tip}(E)$ and $\rho_{sample}(E)$ are both more or less constant for E lying between the tip and sample chemical potentials. Under these conditions $T(E)$ has the form

$$T(E) = \frac{1}{\left((\mu_{tip} - \mu_{sample}\right) \rho_{sample}(E)} \sum_{\psi_n:\ \mu_{tip}<E<\mu_{sample}} M^2 \psi_n \tag{1.8}$$

which allows us to write I as

$$I = \pm\frac{2\pi e}{\hbar} \rho_{tip}(E) \sum_{\psi_n:\ \mu_{tip}<E<\mu_{sample}} M^2 \psi_n \tag{1.9}$$

Now we have a formula for I depending on the matrix elements. Bardeen found a more symmetric expression for them. The idea is to approximate the volume integral in $\langle \phi_j | H - H_{sample} | \psi_n \rangle$ by a flux through a separation surface between the tip and sample.

Choosing any smooth surface in the barrier region that separates the tip and sample and computing the zero operator $H - H_{tip}$ at the tip side

$$\begin{aligned} 0 =& \langle \phi_j | H - H_{tip} | \psi_n \rangle \\ =& \int_T \psi_n(\mathbf{r})(H - H_{tip})\phi_j^\dagger(\mathbf{r}) d\mathbf{r} \\ =& -\frac{\hbar^2}{2m} \int_T \psi_n(\mathbf{r}) \nabla^2 \phi_j^\dagger(\mathbf{r}) d\mathbf{r} + \int_T \psi_n(\mathbf{r}) V(\mathbf{r}) \phi_j^\dagger(\mathbf{r}) d\mathbf{r} \\ & - E_j \int_T \psi_n(\mathbf{r}) \phi_j^\dagger(\mathbf{r}) d\mathbf{r} \end{aligned} \tag{1.10}$$

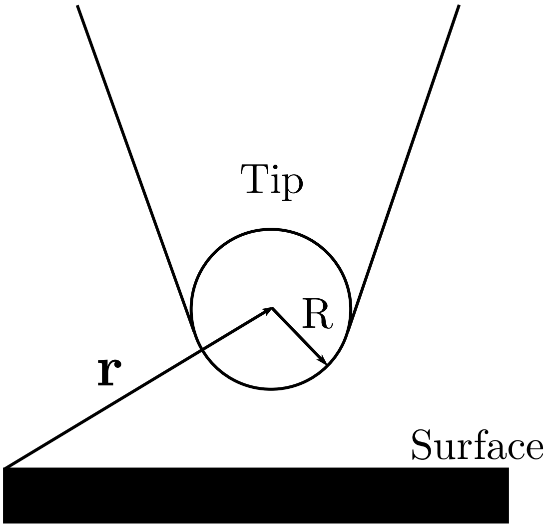

Fig. 1.3 Schematic of spherical tip approximation used by Tersoff and Hamman.

Evaluating $H - H_{sample}$, the zero operator for sample side,

$$\begin{aligned}\langle \phi_j | H - H_{sample} | \psi_n \rangle &= \int_T \phi_j^\dagger(\mathbf{r})(H - H_{tip})\psi_n(\mathbf{r})d\mathbf{r} \\ &= -\frac{\hbar^2}{2m}\int_T \phi_j^\dagger(\mathbf{r})\nabla^2\psi_n(\mathbf{r})d\mathbf{r} + \int_T \phi_j^\dagger(\mathbf{r})V(\mathbf{r})\psi_n(\mathbf{r})d\mathbf{r} \\ &\quad - E_n\int_T \phi_j^\dagger(\mathbf{r})\psi_n(\mathbf{r})d\mathbf{r}\end{aligned} \tag{1.11}$$

where δT denotes the separation surface and T the region consisting of all points on the same side of δT as the tip. Now, subtracting Eq. 1.10 from Eq. 1.11

$$\begin{aligned}\langle \phi_j | H - H_{sample} | \psi_n \rangle &= \int_T \phi_j^\dagger(\mathbf{r})\left(-\frac{\hbar^2}{2m}\nabla^2\psi_n(\mathbf{r}) - E_n\psi_n(\mathbf{r})\right)\right) d\mathbf{r} \\ &\quad - \int_T \psi_n(\mathbf{r}\left(-\frac{\hbar^2}{2m}\nabla^2\phi_j^\dagger(\mathbf{r}) - E_j\phi_j^\dagger(\mathbf{r})\right)\right) d\mathbf{r}\end{aligned} \tag{1.12}$$

In the elastic tunneling regime, i.e., when $E_n \approx E_j$, using Gauss's divergence theorem

$$\langle \phi_j | H - H_{sample} | \psi_n \rangle \approx -\frac{\hbar^2}{2m}\int_{\delta T}\left[\psi_n^\dagger(\mathbf{r})\nabla\phi_j(\mathbf{r}) - \phi_j(\mathbf{r})\nabla\psi_n^\dagger(\mathbf{r})\right].d\mathbf{n} \tag{1.13}$$

where **n** is the normal vector to the separation surface.

In 1983, J. Tersoff and D. R. Hamman applied Bardeen's result to the STM [94]. They modelled the electronic wavefunctions of tip by radially symmetric wavefunctions deducing a rule of thumb: the tunneling current is proportional to part of the electronic density at the center of the tip due to the sample wavefunctions.

Using tip wavefunction of the form

$$\Phi_j(\mathbf{r}) = \mathbf{A}_j \frac{e^{-\kappa_j.\mathbf{r}}}{\mathbf{r}} \tag{1.14}$$

where

$$\kappa_j = \frac{\sqrt{2m|E_j|}}{\hbar} \tag{1.15}$$

which satisfies the time-independent Schrödinger equation for r>R, the tip radii. C. J. Chen [11] provided further insight for $\Phi_j(\mathbf{r})$. It should satisfy

$$-\frac{\hbar^2}{2m}\nabla^2\Phi_j(\mathbf{r}) - E_j\Phi_j(\mathbf{r}) = \frac{\hbar^2}{2m}4\pi\delta_0(\mathbf{r}) \tag{1.16}$$

We can compute $\langle\phi_j|H - H_{sample}|\psi_n\rangle$ in the tip region, getting

$$\langle\phi_j|H - H_{sample}|\psi_n\rangle = -\frac{\hbar^2}{m}2\pi A_j\psi_n(\mathbf{0}) \tag{1.17}$$

where $\phi_j(\mathbf{r})$ in sample region is approximated by $A_j\phi_j(\mathbf{r})$. Rewriting the matrix element

$$M^2(\psi_n) = \left(\frac{\hbar^2}{m}2\pi\right)^2 A^2|\psi_n(\mathbf{0})|^2 \tag{1.18}$$

where A^2 is the average of $|A_j|^2$ over all j such Φ_j is limited in energy to a small range around E_n. In the low bias voltage limit, the tunneling current, I, can be rewritten as

$$\begin{aligned} I &= \pm\frac{2\pi e}{\hbar}\rho_{tip}(\mu)\left(\frac{\hbar^2}{m}2\pi\right)^2 \sum_{\psi_n:\ \mu_a<E_n<\mu_b} |\psi_n(0)|^2 \\ &= (\mu_{tip} - \mu_{sample})\frac{e\hbar^3}{m^2}A^2\rho_{tip}(\mu)\rho_{sample}(\mathbf{0},\mu) \end{aligned} \tag{1.19}$$

where

$$\rho_{sample}(\mathbf{r},\mu) = \frac{1}{|\mu_{sample} - \mu_{tip}|}\sum_{\psi_n:\ \mu_a<E_n<\mu_b} |\psi_n(\mathbf{r})|^2 \tag{1.20}$$

is the sample's local density of states (LDOS) per unit volume per unit energy at the point **r** and chemical potential μ. From here the central idea of STM imaging that tunnel current is proportional to the sample electron density at center of the tip is inferred.

One has to keep in mind that above derived expression is only valid for low bias and low temperature conditions. The Tersoff-Hamman formula is not applicable for e.g., to normally doped semiconductors as a larger bias is required. Nevertheless, Eq. 1.7 provides valuable intuition for spectroscopy and imaging for STM.

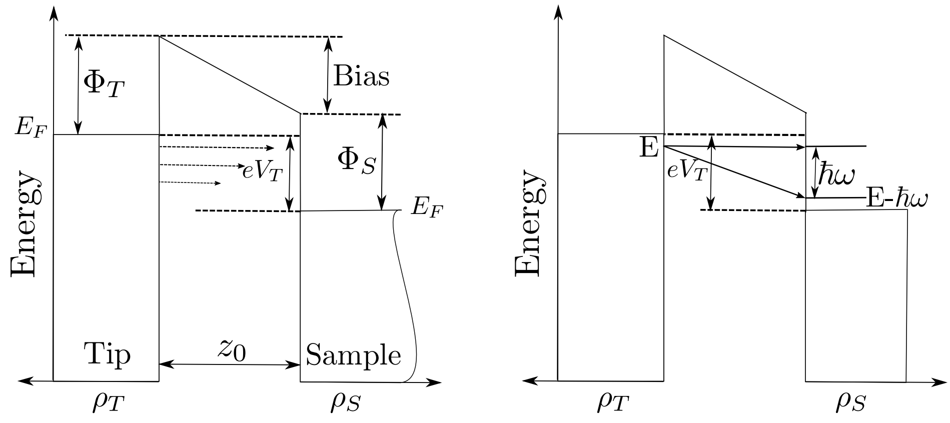

Fig. 1.4 Left. Schematic view of elastic tunneling process. Energy level diagram of an ideal STM tip with a flat DOS, ρ_T, is shown alongwith the sample with LDOS, ρ_S. Φ_T and Φ_S represent the workfunction of the tip and sample, respectively. Under the bias voltage, V_T, the Fermi level is shifted by $\pm|eV_T|$, and electrons are able to tunnel through the trapezoidal barrier formed by the workfunction overlap of tip and sample, and eV_T. Right. Schematic view of potential energy diagram depicting inelastic tunneling process. Magnetic excitaion or molecular vibrations are excited by the inelastically tunneling electrons. The inelastic channel opens when the bias voltage crosses the threshold corresponding to the energy of a certain mode.

1.2 Scanning Tunneling Spectroscopy

STM not only has the imaging capability but also quantitative spectroscopic measurements are possible. Different types of spectroscopies, like dI/dV or dZ/dV, provide information about LDOS of sample and determination of image states, respectively. Here, elastic and inelastic tunneling spectroscopic limits of scanning tunneling spectroscopy (STS) are discussed.

1.2.1 dI/dV

Rewriting Eq. 1.7 for the case of an applied bias between the two conducting electrodes regarding the model presented in Fig. 1.4 at a particular energy ε

$$I = \frac{4\pi e}{\hbar} \int_0^{eV_{bias}} \rho_{tip}(E_F - eV_{bias} + \varepsilon) T(\varepsilon) \rho_{sample}(E_F + \varepsilon) d\varepsilon \tag{1.21}$$

where the tunneling matrix element, $T(\varepsilon)$, over small energy range is constant [11]. Under the assumption that electronic DOS of the tip are constant and some particular values of ε, $\rho_{tip}(E_F - eV_{bias} + \varepsilon) = \rho_{tip}$, can be taken out of the integral. Differentiating

Eq. 1.21 with respect to V_{bias} gives

$$\frac{dI}{dV_{bias}} = \frac{4\pi e^2}{\hbar} T(\varepsilon)\rho_{tip}\rho_{sample}(V_{bias}) \tag{1.22}$$

This means that differential conductance is proportional to the DOS of the sample. By sweeping bias voltage holding the tip (with flat DOS) at constant height spectroscopic information can be recorded in the form of a current signal which is then differentiated. [24, 55, 82] developed further the theory for STS, assuming a constant tip DOS and that the transmission coefficient is to first order independent of bias. Another way is to use the lock-in technique to get the dI/dV signal which is rather noise free and is commonly used. The lock-in technique is discussed in detail in Chapter 2. The lock-in signal can be used to spatially map the differential conductance of a distinct resonance, called the dI/dV mapping. Instead of sweeping the bias voltage it is kept at the energy of a particular state and the lock-in signal is recorded to get spatial distribution of electrons in this state. To ensure good resolution each data point needs to have more integration time than the integration time set for lock-in amplifier. Usually to get rid of tip-sample dependencies and energy dependence of transmission coefficient dI/dV signal is normalized by I/V. It was suggested by Stroscio [89] that the transmission coefficient can be approximated by tunneling current which gives

$$\frac{dI/dV}{I/V} \propto \rho_{sample}(E) \tag{1.23}$$

This is a better approximation for the high bias voltage conditions, i.e., when $|\mathrm{eV}| < \Phi$ no longer holds.

Even though sometimes DOS obtained with STS is identical to the ones obtained by photoemission experiments, it isn't a replacement for them. Since the energy interval accessible in STS is $\approx$ a few eV around the Fermi level because of tip stability issues and electric field influence on local electronic structure [54, 57]. Nevertheless, STS combined with STM can be used to study electronic properties of individual atomic impurities on a surface. The ability to do highly selective spatially resolved analysis makes it one of the most versatile techniques [45, 72, 76].

However, STS does not replace photoemission experiments, especially since the accessible energy interval in STS is usually not wider then ± 4 eV around the Fermi level, due to stability limitations of the tunneling tip and the increasing influence of the electric field on the local electronic structure. Nevertheless, STS in combination with STM is one of the most versatile tools to study the electronic properties of individual molecules on a surface. It allows locating and identifying species at particular sites. Highly selective space resolved analysis can be performed, even where there are several different components present [65] .

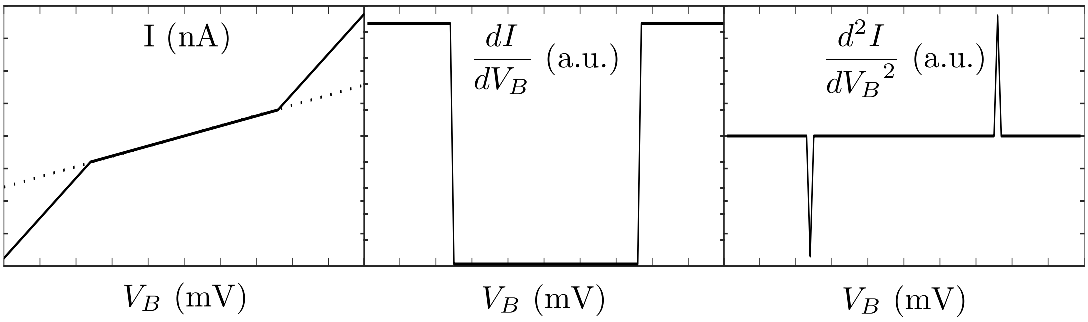

Fig. 1.5 Schematic view of inelastic tunneling process' effect on current-voltage characteristic. Left. The current consists of elastic (dotted) and inelastic contribution. The inelastic channel opens at threshold voltage, $V > \hbar\omega/e$. Centre. dI/dV spectra showing step-like feature, symmetric around E_F. In practise the step is smeared out due to finite temperature effects (not shown). Right. In d^2I/dV^2 spectra dip and peak appear symmetrically around E_F at the voltage corresponding to the excited mode. In practice, the feature would have a width of $5.4\kappa_B T$.

1.2.2 Inelastic electron tunneling spectroscopy

Elastic tunneling is the primary tunneling mechanism at play in STM. The other possibility for the electrons is to tunnel inelastically through the junction [4]. The electrons with sufficient energy give it away during this tunneling process leading to an additional transport path. This energy is absorbed by the environment in the form of, e.g., a vibrational [48, 86] or magnetic excitation [37] as the internal states of adsorbates on the surface are excited. Even after losing their energy partly the electrons still have enough energy to make it to the tip and be detected. Along with the STM's ability to address single atoms, molecules or molecular sites on a surface it can access the inelastic processes for these species.

In Fig. 1.5, schematic of simulated IETS dataset is shown. The inelastic channel provides tunneling path to electrons leading to higher tunneling current. The change in dI/dV can be a bit noisy, leading to d^2I/dV^2 becoming the signal of choice to extract information about inelastic processes at play. The spectra can be understood by taking both tunneling directions in consideration. This turns up as a dip in negative bias voltage, symmetric to the peak on the positive side.

To explain the spectra obtained one has to take in consideration the inelastic tunneling current's contribution which is associated with the release of energy E_i. Using the model as described in [48]

$$I = I_e + I_i \tag{1.24}$$

where I_e is the elastic tunneling current given as in Eq. 1.19 and I_i the inelastic contribution. Now, the tunneling current can be rewritten as

$$I = \sigma_e V + \frac{\sigma_i}{e}\int_{-\infty}^{\infty}\left[F(E-eV+\hbar\omega)(1-F(E)) + F(E)(1-F(E-eV-\hbar\omega))\right]dE \tag{1.25}$$

where σ_e and σ_i are the respective conductances. They define the intensity of the feature coming from respective origins. E.g., σ_i for vibrational feature arising from the electron-phonon coupling. Analytically solving Eq. 1.25 gives

$$I = \sigma_e V + \frac{\sigma_i}{e}\left(\frac{(eV_{bias}-\hbar\omega)f(eV_{bias}-\hbar\omega)}{f(eV_{bias}-\hbar\omega)-1} + \frac{(eV_{bias}-\hbar\omega)f(-eV_{bias}-\hbar\omega)}{f(-eV_{bias}-\hbar\omega)-1}\right) \tag{1.26}$$

where $f(E) = \exp(E/\kappa_B T)$. The first derivative of Eq. 1.26 can be written in a modified form as in [48]

$$\frac{dI}{dV} = \sigma_e + \sigma_i\left(\tilde{f}(-eV_{bias}-\hbar\omega) + \tilde{f}(eV_{bias}+\hbar\omega)\right) \tag{1.27}$$

where $\tilde{f}$ is a modified Fermi-Dirac distribution: $\tilde{f}(E) = (1+\exp(E/1.46k_B T))^{-1}$ [91]. The resulting dI/dV curve exhibits a step increase at $E_F \pm \hbar\omega$ as shown in Fig. 1.5. Now, taking the second derivative leads to an expression which describes the asymmetric dip and peak at $\pm\hbar\omega/e$, as shown in Fig. 1.5.

The d^2I/dV^2 signal is extracted through lock-in detection technique, which will be discussed in detail in Chapter 2. To detect small changes in conductance a relatively long acquisition time is necessary which critically depends on the stability of the STM. The necessary stability conditions, as well as the high energy resolution, can be achieved only at cryogenic temperatures. Apart from the broadening due to the finite temperature, also the modulation voltage broadens the detected signal. Detailed description of the influence of experimental parameters on the STM-IETS spectrum can be found in [63].

1.3 FM-AFM and qPlus

By attaching the STM tip to the prong of a cantilever and recording its deflection, an AFM image can be taken. The forces acting between the tip and sample bend the cantilever providing an indirect access to the interaction force. The ability to investigate insulating samples makes AFM an important technique [26, 62, 93].

qPlus AFM, developed by Franz Giessibl [28, 29], is a version of frequency modulated noncontact AFM. qPlus is considerably better for combined STM/AFM setup because of following reasons:

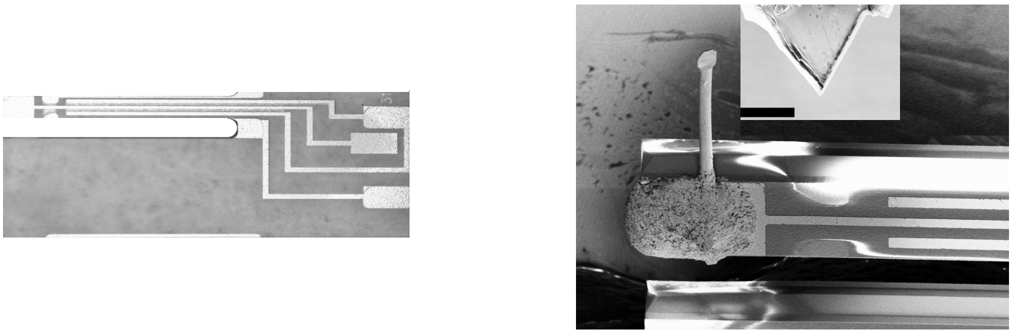

Fig. 1.6 The qPlus design tuning fork and the tip. Left. Optical microscope image of front side of qPlus TF. Right. Scanning electron microscope image of TF with Pt tip glued to it. Inset shows FIB cut Pt wire. Scale bar: 5 µm. Thanks to Matthias Muenks for providing the images. For detailed description of the procedure and assembly please refer to [63].

1. High stiffness ($\approx 1800\,\mathrm{N\,m^{-1}}$) of the cantilever (the tuning fork fixed on the z-piezo is effectively a cantilever) enables its operation at extremely low oscillation amplitudes (< 1 Å). This allows simultaneous STM/AFM operation.

2. The signal is measured directly at the electrodes within the qPlus sensor. Piezoelectric charges generated by deflection of the cantilever dissipate very little power as compared to the conventional cantilevers thus facilitating low-temperature operation. Also, no LASER is required for FM-AFM operation making it perfect for combined functionality with low-temperature STM.

3. Q-factor of the qPlus ($\approx 10^5$) is high enough to achieve good signal to noise ratios in FM-AFM because

   $$\frac{\delta_{thermal}}{f_0} \propto \sqrt{\frac{1}{f_0 Q}}, \tag{1.28}$$

   where f_0 is the natural frequency and Q is the Q-factor.

4. A relatively high resonance frequency ($\approx 30kHz$) keeps thermal noise low (Eq. 1.28).

The following provides a brief theoretical description of qPlus sensors use for FM-AFM. It is based on [62]. The restoring force applied by the cantilever on the tip results in simple harmonic motion with a natural frequency of

$$f_0 = \frac{1}{2\pi}\sqrt{\frac{k}{m^*}} \tag{1.29}$$

where k is the spring constant of the cantilever and m^* the effective mass of the tip. Bringing the tip in proximity to the sample leads to a frequency shift from the natural frequency. For small oscillation of qPlus sensor, the force acting on the tip is assumed to be a linear function of tip height z_0. The frequency of the cantilever can be rewritten as

$$f = \frac{1}{2\pi}\sqrt{\frac{k+k'}{m}} \tag{1.30}$$

where k' is another spring constant between tip and sample. For the qPlus sensor, as mentioned earlier, with high stiffness coefficient implies that Eq. 1.30 can be Taylor expanded. Frequency can be now rewritten as

$$\Delta f = f - f_0 = \frac{f_0}{2k}k' = -\frac{f_0}{2k}\frac{\partial F'}{\partial z} \tag{1.31}$$

which depicts that frequency shift is proportional to negative tip-sample force gradient. Along with all the factors discussed in this section to obtain a good signal to noise ratio a low scan speed is required to get frequency shift images. Pauli repulsion forces, which are responsible for imaging of molecular bonds, can be resolved at oscillation amplitude $\approx$ 1 Å.

1.4 subK STM/AFM

The experimental setup used in this, aka subK STM/AFM [97], is housed in Box 4, Precision Lab of Max Planck Institute für Festkörperforschung, Stuttgart. In Fig. 1.7 a schematic of the setup is presented, and major parts are labeled. Designed as a 14 T UHV STM with ^{3}He cryostat at it was inception in 2005, it has undergone some changes in the pumping system, tip assembly, etc. and is now a combined STM/AFM. Use of ^{4}He instead of ^{3}He for Joule-Thompson cycle limits the minimum temperature to 1.1-1.4 K despite thermal intake from AFM amplifier near the head. The base pressure in both Preparation and STM chambers is $< 5{\cdot}10^{-10}$ mbar. The STM tube is fed in through the STM chamber with cryogenic pumping its base pressure is assumed to be $< 1{\cdot}10^{-10}$ mbar. With vibrational stability provided by the Precision Lab, the z-height stability is better than 1 pm. Preparation chamber houses a sputter gun, heating stage, evaporators and gas inlets, and Auger electron spectrometer and mass spectrometer, providing a broad range of in-situ sample preparation possibilities. The superconducting magnet sits around the STM tube, in liquid He bath. `Nanonis` from `SPECS GmbH` is used as the control electronics and software for the STM/AFM operation. The tunneling current is amplified using a variable gain (10^3-10^{11} V A^{-1}) low noise current-to-voltage amplifier from `FEMTO Messtechnik GmbH` (`DLPCA-200`).

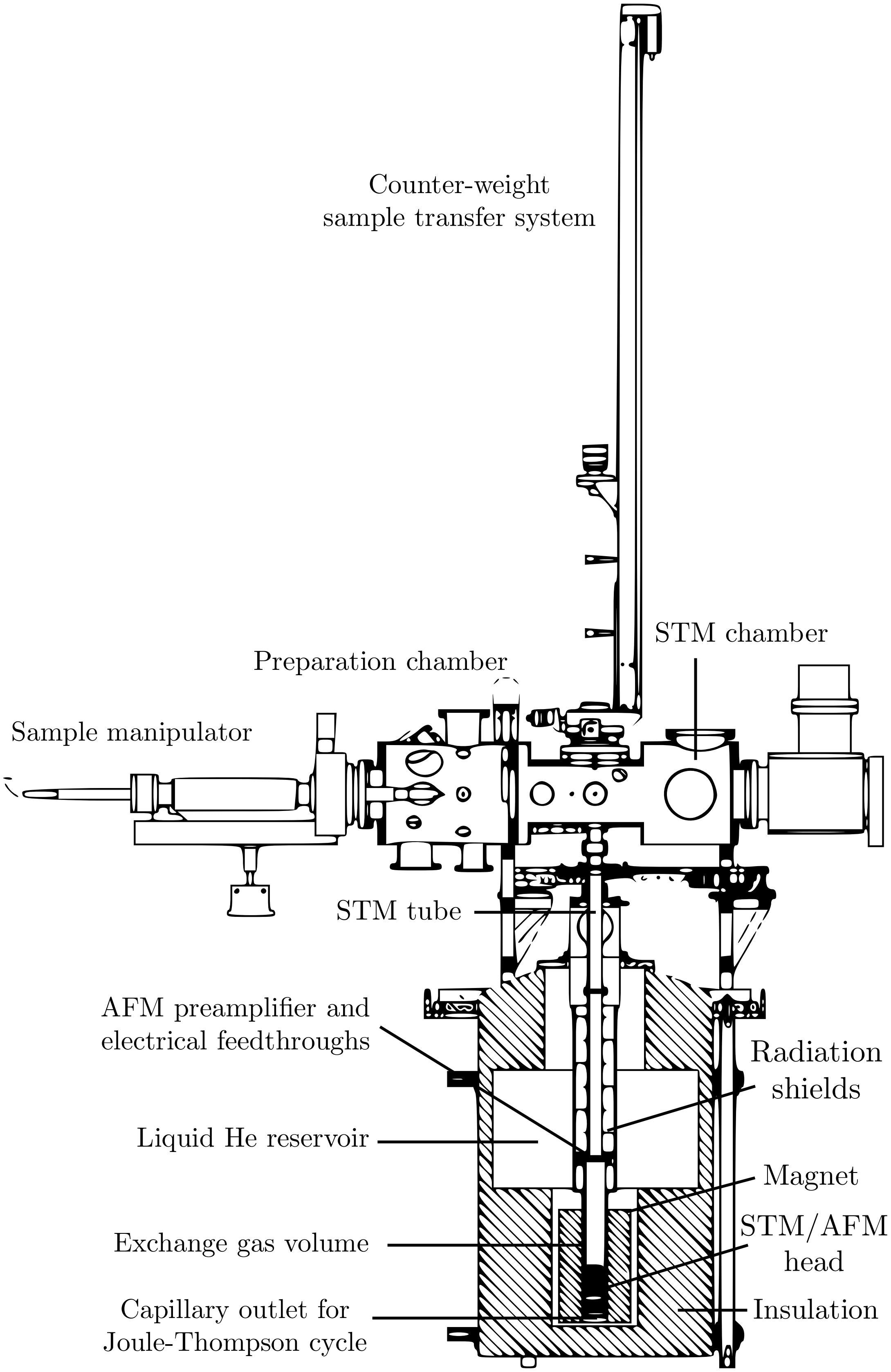

Fig. 1.7 Schematic of subK STM/AFM showing all the major components

The unavoidable trade-off of working at cryogenic temperatures, the measurement time between two filling cycles, is ≈ 60 h.

1.5 Sample holder

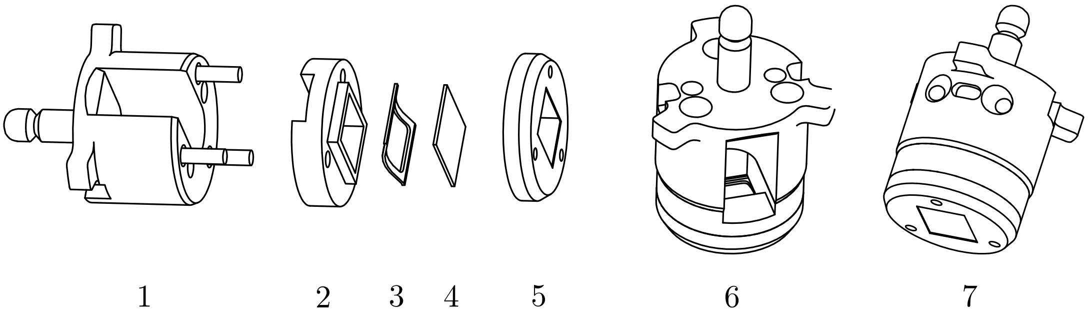

Fig. 1.8 CAD overview of the modified sample holder for bulk insulating samples. 1. depicts the old sample holder part with screw assembly ports. 2. shows the base of the cap where sample sits. 3. is the spring to push sample against the cap to maintain good contact. 4. is the SiC wafer. 5. shows the cap that pushes the whole assembly together using M1.4 Molybdenum screws. 6. and 7. are overview of the assembly from different angles.

Work done on a bulk insulating sample, like SiC in this thesis, required small alteration in the sample holder design. The bulk metal samples, like Cu (111) or Rh (111) are pressed against the Molybdenum sample holder from all sides to form good electric contact. The graphitized SiC(000-1) has to be electronically contacted from the top and is fragile. This requires that it be contacted from the top by a cap (shown in Fig. 1.8, which is thinned down to 100 µm. The sample is pushed into the cap by a Molybdenum wire spring to ensure good contact while the sample undergoes annealing to 900 K during preparation and cryogenic cooling to 1 K during measurement.

Chapter 2

STM tip approach optimization

To begin the measurement after a new sample has been cooled down to the base temperature, the STM tip has to be moved from the back contact (safe position) to the tunneling regime. This involves moving the tip from ~5 mm to a few angstroms away from the sample safely, avoiding any contact with the sample's surface. In the following section optimization of the tip approach for scanning probe instruments with no optical access or absolute tip-sample distance readout is discussed.

2.1 Tip approach mechanism

Using the control electronics a slip-stick drive is used to move the coarse piezo-tip assembly towards the sample. This can be realized in two ways: 1. the tip-sample distance (z) is reduced (Δz~50 nm, for subK STM/AFM) by a step, followed by a feedback check to detect tunneling current. These steps move the tip towards sample until a tunneling current is detected; 2. reducing z continuously while the feedback detects a tunneling current. Even though the latter method is faster, it's unreliable as the control electronics are not usually fast enough to prevent a tip-sample contact. This makes the former mechanism to be a more popular way of approach[1]. Several coarse approach mechanism to increase the reliability of the motor has been developed since the invention of STM. Our STM/AFM head (for design details see [39]) uses *the walker* type developed by Pan and coworkers [69]. A tube scanner is placed inside a sapphire prism mounted by six pieces of shear piezo stacks. These are first moved simultaneously in the sample direction by applying a fast voltage ramp. The sapphire prism stands still until all the shear piezos have been moved to the new position (slip part). After which the applied voltages on all the shear piezo stacks are reversed slowly

---

[1] The procedure followed by us involves bringing the tip from back contact to a few µm away from the sample surface using continuous coarse steps followed by switching to the auto approach protocol. This switch between the two modes is governed by a reference lock-in value which is known for a particular sample.

but simultaneously. The sapphire prism then follows the synchronized move of all the shear piezo stacks (stick part).

For our STM/AFM, since the tip is glued on a quartz tuning fork, each step leads to an impulse which makes the tuning fork oscillate. Oscillating tip translates into extra cautious, slow approach. E.g., each auto approach step, where the tunneling current is checked after every step, has to have an added delay of 2-5 s for SiC(000-1) sample at 5 K. This translates into a very long approach time being ~several hours assuming 1000-2000 steps for such samples.

Since our system does not have optical access to the STM head, a conventional optical coarse approach, to reduce z to a few µm is not possible. Another possible approach is using a reference capacitance value ($\propto$ Lock-In signal) as the limit of the coarse approach and then starting the automatic approach protocol (mention reference) to reach the tunneling regime. But this reference capacitance value is highly dependent on the geometrical capacitance of the sample holder-tip geometry. This implies that minor changes in sample holder geometry, from Au(111) crystal in head form to cleaved $NbSe_2$ samples to top contacted SiC(000-1) lead to different reference capacitance values. This change in reference capacitance values renders the "reference" useless.

Recently, de Voogd *et al.* [17] reported a capacitance vs z calibration method where they calibrated the approach mechanism using the reference curves obtained using precise capacitance bridge measurements. But this method also relies highly on reliability of the coarse motor and a constant sample geometry. Instead of relying on the calibration one could select a certain threshold in capacitance vs z characteristics and use a routine for control electronics to detect it and switch from fast coarse approach to slow auto approach. Schlegel *et al.* [79] used the aforementioned approach to optimize approach time for their dip-stick STM. They used the analog lock-in amplifier to access the tip-sample capacitance. The next section provides a brief description to how the lock-in works and how it can be used to access the tip-sample distance.

2.2 Lock-In technique

As mentioned before, instead of numerically differentiating I(V) to obtain dI/dV, a lock-in amplifier is used. This has many advantages, including:

1. Reduced 1/f noise
2. Spectral purity not required, i.e., noise at certain frequencies, e.g., 50 Hz do not influence the results
3. Numerical differentiation not required

For these reasons, lock-in technique is usually used for spectroscopic measurements. It involves applying a sine wave, $\sin(\omega_0 t)$, on top of the signal, integrate over a period, and recover the signal at ω_0.

Let the signal, $f(t)$, by Fourier decomposition, be:

$$f(t) = \frac{B_0}{2} + \sum_{n=1}^{\infty} A_n \sin(n\omega_0 t) + B_n \cos(n\omega_0 t) \tag{2.1}$$

where $\omega_0 = 2\pi T$. A_n and B_n are obtained by multiplying this by $\sin(m\omega_0 t)$ or $\cos(m\omega_0 t)$ and integrating it over one period. A lock-in multiplies Eq. 2.1 by the reference signal, $\sin(n\omega_{ref} t + \phi)$, integrates it over one period, and multiplies the result by $\frac{\omega_0}{\sqrt{2}\pi}$:

$$V_{lock-in} = \frac{\omega_0}{\sqrt{2}\pi} \int_{t_0}^{t_0+2\pi/\omega_0} f(t) \sin(n\omega_{ref} t + \phi) dt \tag{2.2}$$

Setting $\omega_{ref} = \omega_0$ and $\phi = 0$,

$$V_{lock-in} = \frac{1}{\sqrt{2}} \cdot \frac{\omega_0}{\pi} \int_{t_0}^{t_0+2\pi/\omega_0} f(t) \sin(n\omega_0 t) dt \tag{2.3}$$

which means that lock-in measures the Fourier component of the signal, at the set modulation frequency. The $I(V)$ signal consists of a resistive and capacitive part which is 90° out-of-phase concerning the resistive signal. With the tip out of tunneling, the phase is tuned such that all of the signal is in one of the two channels, either X or Y. The resistive signal is then in the other channel. Rewriting Eq. 2.2, using Fourier decomposition form in Eq. 2.1

$$V_X = \frac{1}{\sqrt{2}} \left(B_n \sin(\phi_n) + A_n \cos(\phi_n) \right) \tag{2.4}$$

$$V_Y = \frac{1}{\sqrt{2}} \left(B_n \cos(\phi_n) - A_n \sin(\phi_n) \right) \tag{2.5}$$

where ϕ_n and $\phi_n + \pi/2$ are the phase for V_X and V_Y, respectively. Instead of performing a one-period integration, a real lock-in passes the signal through a low-pass filter, which is a good approximation to integration in Eq. 2.4,2.5.

Applying modulation voltage $\Delta V = A_m \sin(\omega_m t)$ to the tip-sample junction, the voltage output of pre-amplifier is [9]

$$f(t) = \frac{I(V + \Delta V)}{G} \tag{2.6}$$

where G is the gain of the pre-amplifier ($G = 10^{-9}\,\mathrm{A\,V^{-1}}$). Since the lock-in measures the Fourier component of this signal,

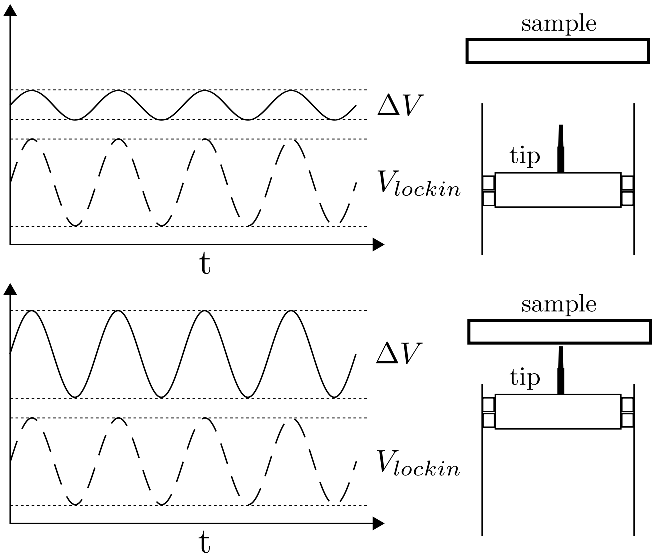

Fig. 2.1 Principle of capacitive coarse approach. V$_{bias}$ is modulated by the signal V_{lockin} (Modulation amplitude = 10 mV; Modulation frequency = 607 Hz). For small z response signal ΔV has higher amplitude (Bottom) as for large z (Top).

$$I(V+\Delta V) \approx I(V) + \frac{dI}{dV}\Delta V \tag{2.7}$$

where, for the correct phase,

$$\frac{dI}{dV}\Delta V = A_n \approx \sqrt{2}V_X \tag{2.8}$$

Thus, the analog output of the lock-in is

$$\frac{dI}{dV} \propto \frac{G}{\Delta V}V_0 \tag{2.9}$$

where V_0 is the actual voltage reported by `Nanonis`. Using the capacitive component of the $I(V)$ signal the junction capacitance can be measured [9].

2.2.1 Using lock-in for tip approach optimization

Using the apparent current, related to capacitance of the junction, the relative position of the tip with respect to sample can be known. The tunneling current is amplified to an AC voltage signal whose amplitude depends on junction impedance. Thus, variation of amplitude of the lock-in signal in our capacitive channel depends tip-sample gap (see Fig. 2.1).

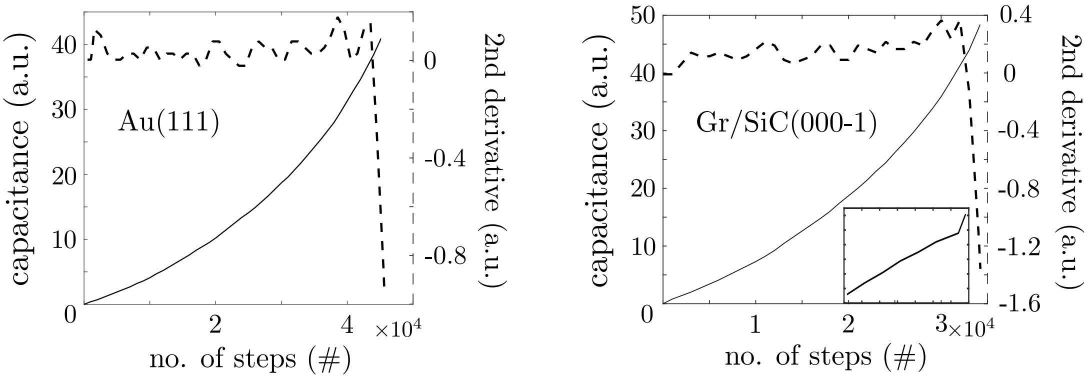

Fig. 2.2 dI/dV vs z behavior. dI/dV vs z characteristics on Au(111) (Left) and Gr/SiC(000-1) (Right) sample is shown. The dashed line depicts the second derivative of the dI/dV vs z characteristics. Inset. A zoom in on the kink appearing in capacitance vs z characteristic at $z \approx$ 1-2 μm

2.3 Analysis of tip-sample capacitor

Here, the data obtained for approach on Au(111) and Gr/SiC(000-1) sample is analyzed to get an insight into dI/dV vs z characteristics (see Fig. 2.2). The overall upward concave curves, for large z, show close to linear behavior. But as the tip gets closer to the sample ($20 \times 10^3 \gtrsim \# \gtrsim 2.5 \times 10^3$) the wiggles in the curvature (as seen in the second derivative) appear. When the tip gets close enough to the surface a large change in curvature, which translates into large negative step in the second derivative, is observed for all samples and different sample holders. The measurements were done at both 5 K and 1.2 K show the same qualitative behavior as shown in Fig. 2.2.

By looking at the curvature of the characteristics a protocol for control electronics can be designed which detects the change in curvature as the z is decreased. By selecting a certain threshold for change in curvature for switching from coarse approach to auto approach, STM pre-approach time can be significantly reduced. For subK STM/AFM, using the above procedure pre-approach time has been reduced to ~30 min. Since the method relies only on tip-sample capacitance, it can be easily expanded to any scanning probe instrument which requires the pre-approach.

Chapter 3

Local work function variations on *h*-BN/Cu(111)

The work function, defined as the minimum energy required to remove an electron from the surface to infinity, is a fundamental property of a surface. It affects the reaction mechanisms and catalysis at the surface due to local variations of charges [95]. Any adsorbed species, sub-surface defects, or nano-patterning can lead to variable charge distribution on the surface. Lateral electric fields or local doping [74] owing to charge distribution affects properties of adsorbate [50]. However, Φ values measured by most of the radiation-based methods are averaging over large areas (few µm). Probing Φ from a relatively larger distance than the surface area of interest leads to the averaging of net charges that occur due to Φ difference. The nanometer scale resolution of STM, which radiation- and transport-based methods are still lacking [50], makes it an attractive technique to probe Φ variations. The *h*-BN/Cu(111) surface which is an excellent template for studying self-assembly, magnetic adsorbates [51] is an interesting candidate for studying Φ variations and comparing them with other methods and theory. In this chapter, the combined STM/AFM functionality of our instrument is used to study these variations using field emission resonance (FER) states and Kelvin probe force microscopy (KPFM). In this chapter the experimental parameters used to grow *h*-BN on Cu(111) are discussed, followed by a Φ variation study using two independent techniques.

3.1 *h*-BN on Cu(111)

Monolayer *h*-BN on Rh(111) has been the work horse of our group for studying magnetic excitations in CoH_x systems [41, 46, 47, 64] over the last years. Even though the high catalytic activity of Rh(111) makes it easier to grow *h*-BN, the lattice mismatch between *h*-BN and Rh(111) leads to a structural corrugation which makes it harder to manipulate adsorbates. Manipulability of adsorbates is an important aspect, as the complexity of experiment rises. Moreover, *h*-BN on copper foil being a model system for industrial production of BN makes it important from a technological point of view [51].

3.1.1 Preparation

The preparation of *h*-BN on Cu(111) begins with obtaining a clean Cu(111) surface. The Cu(111) crystal is prepared by repeated cycles of sputtering with Ar^+ ion (60 min at 1.5 kV) and annealing up to 980 K for 15 min in ultra-high vacuum. To control the success of this procedure the Cu(111) crystal was checked in the STM. A clean Cu(111) surface with large, flat terraces was obtained with only a few sulfur impurities. The *h*-BN is then directly grown by chemical vapor deposition in the preparation chamber of our instrument. Borazine ($(HBNH)_3$) is dosed through a leak valve at a pressure of 2×10^{-7}mbar at sample temperature of 1000 K for 10 min to obtain roughly a full monolayer. Afterwards, the temperature is slowly lowered to allow uniform growth of the layer before the sample is transferred in-situ to the cold STM head. Using the same parameters but only 2 min dosage time we obtained partially coverage which allows for better tip preparation. This might also be advantageous for controlled manipulation of atoms or molecules.

3.1.2 Structure and electronic properties of *h*-BN/Cu(111)

h-BN forms an at least electronically corrugated sheet above the Cu(111) surface with a hexagonal Moiré superstructure with periodicities ranging from 3 nm to nearly 15 nm. This can be verified by using simple geometrical model overlay *h*-BN (lattice constant = 2.5 Å)and Cu(111) grid (lattice constant = 2.56 Å) [15]. Two hexagonal grids are overlaid with a set mismatch in lattice constant and rotated with respect to each other at small angles two reproduce Moiré superstructure for the case of *h*-BN/Cu(111). Moiré superstructure periodicities obtained by the above method did not correspond to experimentally obtained ones for both 2% lattice misfit or the 0% misfit for stretched *h*-BN as described in [51]. Here, in the presented data, for misfit of 1.8% with minute rotation angles between the two grids could reproduce periodicity and orientation of Moiré superstructure. Fig. 3.2 shows STM topography image of *h*-BN/Cu(111) at high and low positive bias voltage. There is a considerable electronic corrugation because of the lattice mismatch to the substrate. Compared to *h*-BN/Rh(111), this superstructure, at least in our data, not linked to mechanical corrugation [20]. This makes *h*-BN/Cu(111) attractive for atomic manipulation possibilities. The electronic

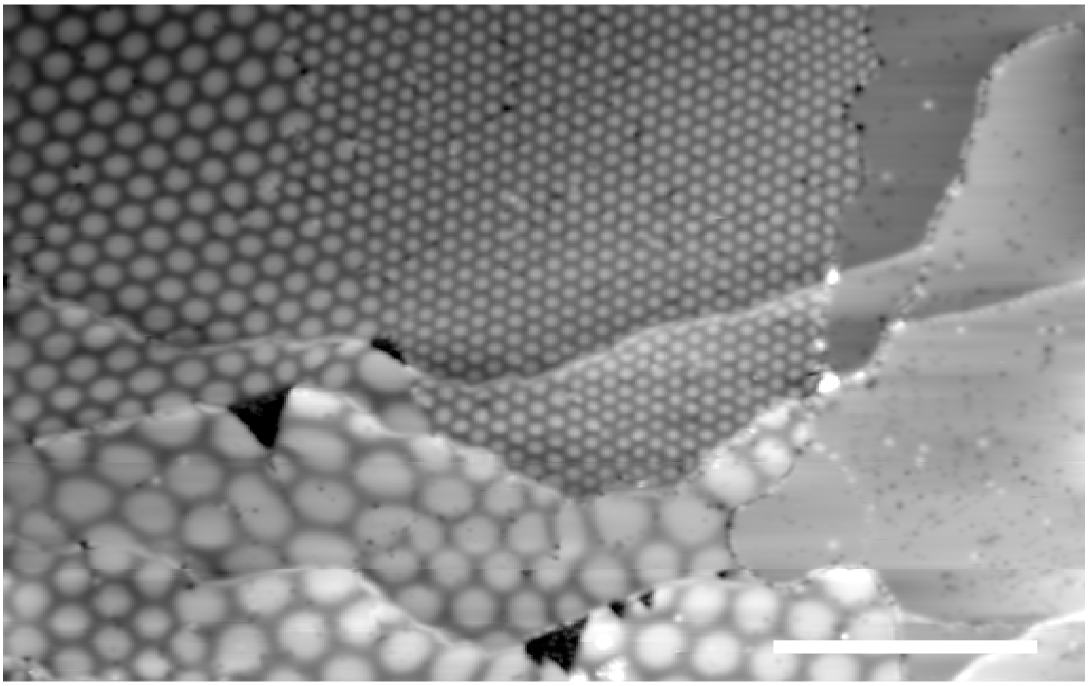

Fig. 3.1 Large scale (200 nm × 125 nm) constant-current STM image of *h*-BN/Cu(111). I = 20 pA and V_{bias} = 3.7 V. *h*-BN grows over the step edges of underlying Cu(111) surface. Different relative rotational orientations of the Van der Waals layer with respect to the substrate lead to varying Moiré-like superstructure.

corrugation leading to trapping potentials for atomic and molecular adsorbates makes it unique compared to other decoupling layers.

For structural analysis STM topography of *h*-BN/Cu(111) was taken at V = -5 - +7 V. Different apparent heights of *h*-BN on Cu(111) substrate was obtained for different bias voltages which shows a nice example to the known fact that STM is unable to detect the true topographic height. Due to *h*-BN being insulating, no spectroscopic contribution is expected from it within the band gap. This makes it transparent to STM at low bias voltages, as seen in Fig. 3.2(d). Friedel oscillations [36] due to the scattering of the Cu(111) surface state are observed on *h*-BN with a marginally larger wavelength. The dI/dV map for the two bias voltages shows electronic structure of the Cu(111) substrate for the low bias voltage and corresponds to Moiré superstructure at a high bias voltage. The interface state occurring at these high positive voltages lead to the Moiré pattern seen in dI/dV [8]. It should be noted that the latter does not correspond to an intrinsic *h*-BN related band, but only represents a modification of the Cu(111) surface state upon *h*-BN adsorption. One to one correspondence can be seen between frequency shift images, obtained simultaneously with STM topography, and STM image. However, at low bias voltages due to constant current imaging mode, one can still see the Friedel oscillations near the rim sites. The height z was modulated

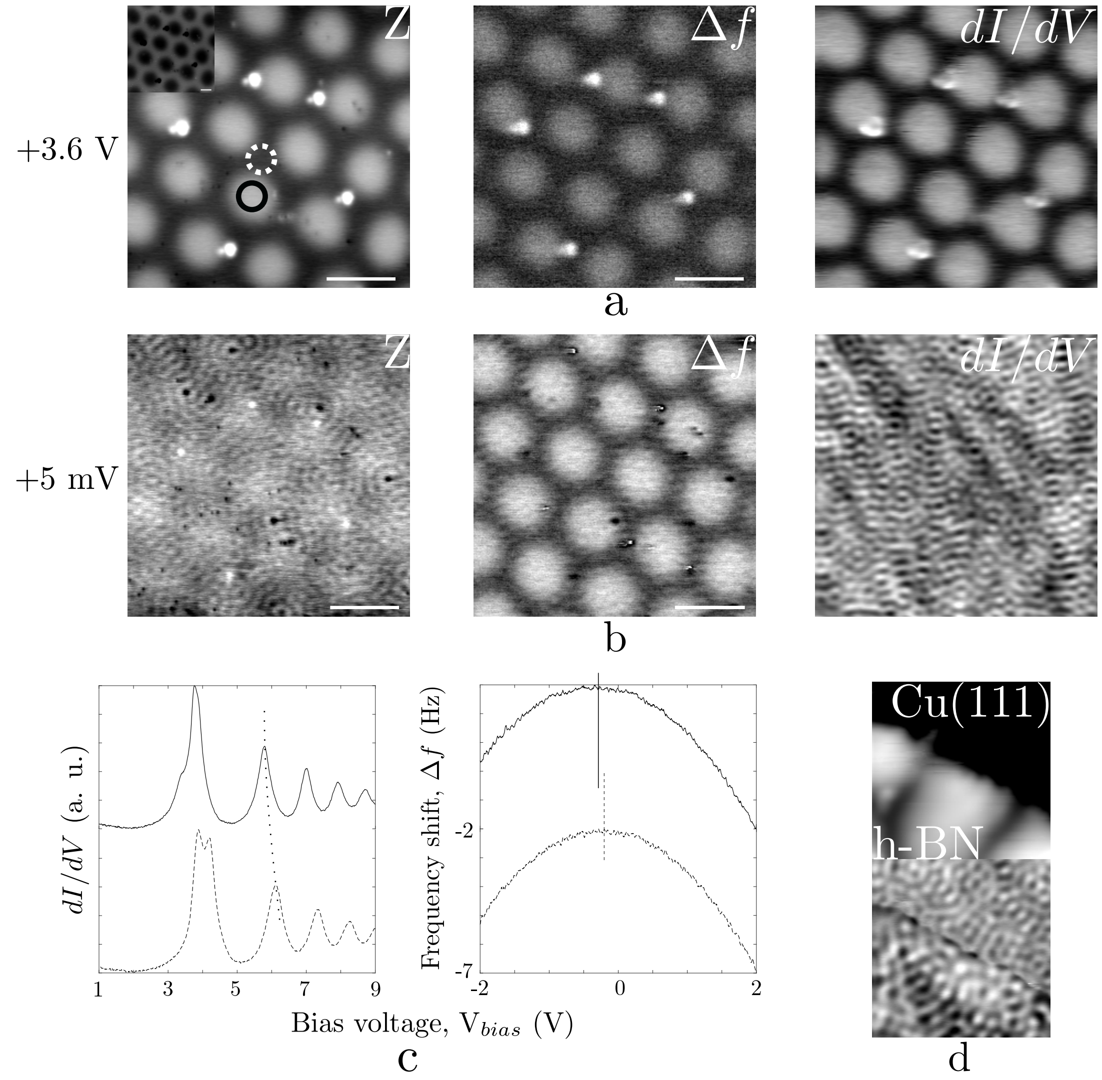

Fig. 3.2 Structure of *h*-BN/Cu(111). a.) Left. STM topography at V$_{bias}$ = 3.6 V. Inset. STM topography at V$_{bias}$ = 4.8 V. The circles (line and dotted) mark the valley and bridge sites. Center. Frequency shift image. Right. dI/dV map of the area. b.) Same as a.) with V$_{bias}$ = 5 mV. c.) FER and KPFM measurement at valley and bridge region. d.) STM topography of the *h*-BN/Cu(111) interface at the two bias voltage values. Scale bar: 10 nm. Current: 500 pA

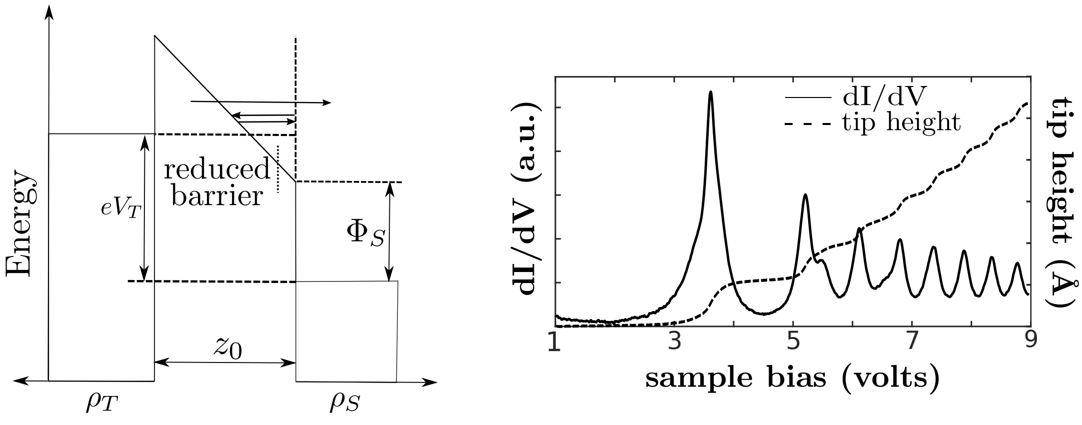

Fig. 3.3 Field emission resonance. Left. Schematic of tunnel junction under high sample bias. The triangular potential barrier can host eigenstates which aid occurrence of transmission resonances. Right. Constant current dI/dV measurement and corresponding tip trajectory measured on *h*-BN/Cu(111).

by the STM feedback influencing the AFM channel. At higher bias voltages (+4.8 V) contrast inversion in the STM topography occurs as shown in the inset of Fig. 3.2. The apparent corrugation and contrast inversion at these bias voltages is related to the emergence of the first FER peak.

For the bare Cu(111) region dI/dV measurement show surface state onset at -440 meV, which corresponds to the literature value [75, 77]. On *h*-BN adsorbed regions the onset occurs at about -330 meV, showing that the band is upshifted by nearly 100 meV. Comparing the shift in band below *h*-BN to other adsorbates like NaCl/Cu(111) (230 meV) [77] and Xe layer on Cu(111) (130 meV) [71] suggests weak interaction to the substrate.

3.2 Work function using STM/AFM

In this section, local Φ variations on *h*-BN/Cu(111) are discussed. The two techniques FER maps and KPFM maps were used for the purpose above. A brief overview of the two methods is provided. Later, the two are compared concerning their resolution, and an estimate of the Φ variation on *h*-BN/Cu(111) is provided.

3.2.1 Principle of FER

Under high bias voltage conditions, the tunnel junction potential in a 1D simplification looks like Fig. 3.3. The electrons find themselves in a triangular potential well formed by the junction boundary and its electric field. Whenever the electron energy coincides with an eigenstate of the well, a transmission resonance can occur [35]. For a flat metal surface, the FER states, delocalized in the surface plane, consists of a band of a 2D electron gas. In STM, one can use dI/dV spectroscopy to access the FER states. The measurement is performed by ramping bias voltage while keeping I constant, recording the z and dI/dV value throughout. When the voltage reaches the energy of an FER state, the tip retract instantly by ~1 Å per state. The energy values of these curves can be clearly seen in the dI/dV curve as shown in Fig. 3.3. Due to the strong electric field at the STM junction for such high bias voltages, the energy spacing between two states is distorted because of Stark shift [13, 22]. The Stark shifted image potential states seen in dZ/dV curve are referred to as FER states.

The FERs are weakly coupled to the metal substrate because of being so close to the surface. Their energies are determined with respect to the vacuum level. This means that variations in the energy of FERs are related with variations of local Φ [73, 74]. For higher biases, because of the high electric field at the junction, the Stark shift is stronger. This means that Φ variations are ascribed according to the variation of the first FER. Because of the high bias voltages involved this technique is not suitable for use on molecules because they are unstable at such high biases. The positive bias voltage on the sample reflects the FER on the sample because the electrons tunnel from the tip to the surface. At negative bias values, the FER represent the tip state. Thus, to probe local Φ variations high positive bias voltages are used. STMs capability of being a local probe is advantageous here as well as FERs can be probed at specific positions. This means that they do not suffer from broadening due to summation over different structures for radiation-based techniques.

3.2.2 Principle of KPFM

The AFM tip scanning over the surface has a different Φ than the substrate. Due to the dipole layers formed on the substrate and the tip it will experience electrostatic forces. This is a consequence of the difference in Φ, called the contact potential difference (CPD) [61]. For a conductive tip, the electrostatic force can be compensated for when the bias applied to the junction compensates for CPD [66]. For FM-AFM the forces involved lead to a frequency shift. For a KPFM measurement, the tip oscillates at a frequency, ω, and the potential difference between tip and sample is

$$V = (V_{bias} - V_{CPD}) \tag{3.1}$$

where V_{bias} is the bias voltage applied to the sample, V_{CPD} is the CPD. Approximating the tip-sample junction as a parallel plate capacitor, the force can be written as

$$F = \frac{1}{2}\frac{dC}{dz}V^2 \tag{3.2}$$

where C is the capacitance between tip and sample and V potential difference. Substituting V from Eq. 3.1, the frequency shift, $\Delta f \propto dF/dz$ can now be written as

$$\Delta f(V) = \frac{d^2C}{dz^2}\left(V_{bias} - V_{CPD}\right)^2 \tag{3.3}$$

For V_{bias} equal to the CPD, F is equal to zero. Accessing CPD in this way is known as KPFM. Accurate Φ values can be determined if the tip is calibrated by measuring the CPD on a surface of known Φ. In the absence of an exact calibration, CPD variations measured on a surface allow one to determine Φ variations, as the Φ of tip is constant during the measurement and variations arise only due to variations of the local Φ of the surface.

3.2.3 FER maps

FERs can be observed in STS as peaks in dI/dV spectra taken in constant current mode. However, not every peak observed at high positive bias voltage reflects an FER state (see Fig. 3.2). The lowest peak observed on *h*-BN/Cu(111) is an interface peak similar to the one observed on Gr/Ru(0001) [8, 87]. This peak occurs because of the interface state localized between the *h*-BN and Cu(111) surface. The peak is smoother than the other peaks observed and varies little in energy (~40 meV). This small variation in Φ can be attributed to corrugation of the *h*-BN/Cu(111). The proximity effects in the adlayer could lead to these variations and shape of the peak. The proximity of Graphene to Ru(0001) shifts the interface peak to higher energies than obtained here [8, 87]. This also explains the variation observed between the rim/bridge and valley region. Therefore, the second peak observed in dI/dV spectra is addressed as the first FER in the following.

To map the FERs, a grid of points is overlaid on the area of interest (see Fig. 3.4). At each of these points the bias voltage is ramped from 1 V to 9 V while keeping the current constant (I = 100pA). The dI/dV curves spanning the first FER are arranged in a 2D matrix which can be used to obtain a colormap for each bias value. These images can then be put together into a movie showing maps at gradually increasing bias. In Fig. 3.4(d), frames of such a movie are shown. A striking observation from these movies is the appearance of a bow-like structure in the valley for increasing bias. This effect can be attributed to the asymmetric tip shape leading to different Φ values at the tip. Presumably, due to the local directional gradient two facets of the tip with different Φ contributing to the tunneling current lead to this shape. The sharpness and intensity of the FER peaks in the valley region make it possible to look at this Φ. At higher voltages, rings start to appear around the valley, and rim regions brighten up gradually [18]. At even higher bias values the peak undergoes contrast inversion.

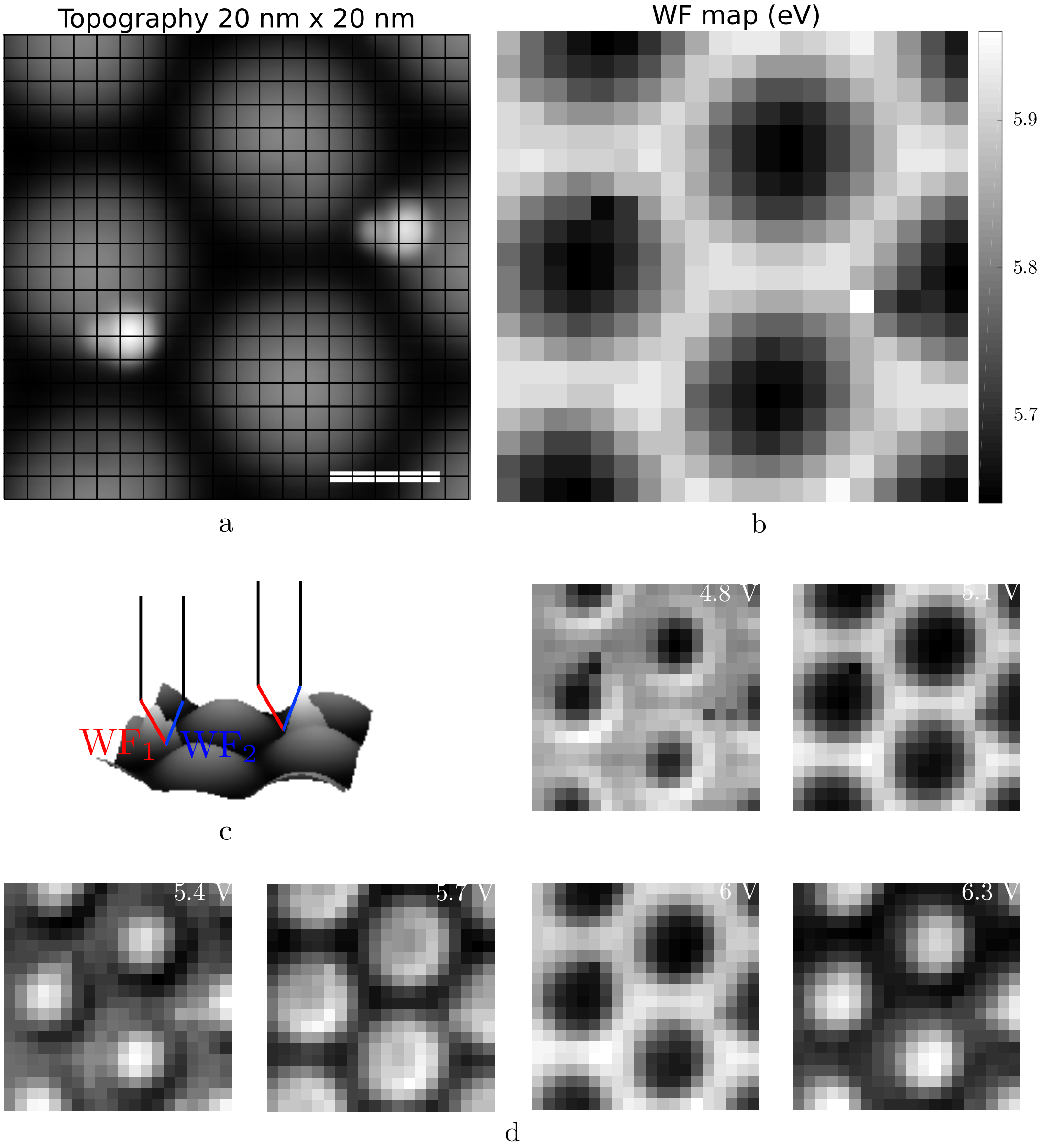

Fig. 3.4 FER map of *h*-BN/Cu(111). a.) STM topography of the area with overlaid 20 x 20 grid. Scale bar: 4 nm. b.) Φ variation colormap using the shift in first FER peak. c.) Scheme of the tip Φ effect on local FER measurement. d.) Energy slices of first FER peak showing the asymmetric onset of the state. Scale bar: 5 nm

Assuming constant Φ throughout the valleys a map of the first FER can be obtained (Fig. 3.4(b)).

Fitting sum of two Gaussian peaks, to better capture the form, to the first FER peak the maxima can be calculated for each of the grid points. Converting this again to a 2D matrix a colormap showing variation in peak energy values can be obtained. In Fig. 3.4(b), such a map is shown. The absolute difference between the shift in first FER peak between rim and valley is 245 mV. A histogram of peak positions at the two areas was plotted and fitted by a Gaussian. The difference between the two peak positions gives Φ variation between rim and valley to be 142 ± 11 meV.

The map obtained at $V = 5.7$ V shows ring features developed in the valleys (Fig. 3.4(d). Lowering of Φ in the valley might lead to the formation of a standing wave mode, similar to the one responsible for FER, could be responsible for such a ring-feature [21]. For such a case the first FER peak would also have a double peak like feature.

The ring-like feature around the valley centers (e.g., 5.7 V colormap in Fig. 3.4(d)) reflects a standing wave mode which the valley region can sustain due to its lower Φ. This could be similar to a circular potential well which can sustain several electron eigenstates [34]. Wavefunction for such a system can be written, using quantum numbers n and m, as

$$\psi(n,m) \propto J_m\left(\frac{r}{r_m^n}\right).\sin(m\phi) \tag{3.4}$$

where J_m is the m^{th} Bessel function in the radial direction (r), truncated at its n^{th} zero (r_m^n). This is then multiplied by a sinus function in the azimuthal coordinate (ϕ). Quantum numbers n and m describe a number of nodes in radial and azimuthal direction respectively. For this system, the (0,1) mode ($n = 1$, $m = 0$) is the one with the lowest energy and is reflected by a peak inside the valleys, peaking at their center. In the experimental data, this is seen as a wave-like feature traveling through the center of the valley. Colormap corresponding to the bias voltage of 5.4 V in Fig. 3.4(d) reflects the state across the entire valley but is also reflected in the maps around said bias voltage. (1,1) mode is the next mode for the circular disc problem and has two peaks with opposite sign at opposite side of the disc. For the case of tunneling into states with varying nodal diameter and its different orientations, a ring-like feature is expected [14]. The case of bias voltage 5.7 V) shows a ring-like feature corresponding possibly to the (1,1) mode.

3.2.4 KPFM maps

Similar to the FER measurement a grid is laid on the surface to mark the measurement positions. To be able to compare resolution of the two techniques same grid size (20

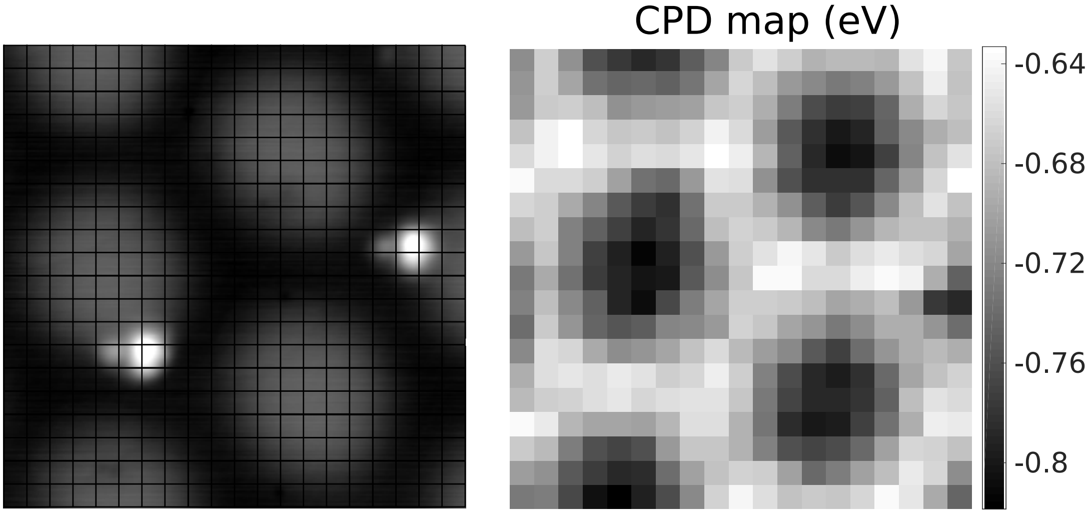

a b

Fig. 3.5 Φ variation using KPFM. a. Topography of the area prior to KPFM measurement. b. Colormap of the CPD obtained using constant height KPFM map or the area.

× 20) was used. At each of these grid points, the tip is placed in constant height mode, and the frequency shift is recorded as the bias is ramped from -2 V to +1 V. Between two measurements the tip is moved to the center of the valley and the feedback loop is switched on to readjust tip height. This avoids overall drift of the z-piezo over the several hours of measurement time. Fig. 3.2(c) shows KPFM measurement for the case of rim and valley region. Additional electrostatic forces lead to an offset of the entire curve which translates to $\Delta f(V_{CPD})$ not being identical for rim and valley measurement.

A MATLAB code was used to perform parabolic fit and extract the maxima of $\Delta f(V_{bias})$ curve. The values obtained for V_{CPD} are then used to obtain colormap shown in Fig. 3.5(b). The absolute difference between the valley and rim V_{CPD} positions was found to be 185 meV. A histogram of the V_{CPD} values for rim and valley areas was generated and fitting Gaussian to the data gives a Φ variation between rim and valley to be 62 ± 14 meV. As is seen in Fig. 3.5 the areas of high CPD appear lower in topography. This observation is in qualitative agreement with the FER maps obtained in the same area. Two defects were seen in Fig. 3.5(a), not visible in CPD map, reflect upon the fact that KPFM measurement has a poor lateral resolution. It relies on long-range electrostatic interactions which results in weighted average over the relevant size of tip (~5-10 nm) [100]. This also leads to averaging effects in CPD map between the rim and valley regions since they are also in this size range. In total, this leads to an underestimation of the Φ difference value measured by this technique. Nevertheless, areas with lower and higher Φ values are discernible and in agreement with the previous measurement.

Table 3.1 Calculated and measured Φ variation on *h*-BN/Cu(111)

Method	Φ variation (meV)	Reference	Comment
Approach curve	300	[51]	local measurement leads to more pronounced shift T = 6 K
FER maps	143±11 (245)	present work	closest estimate provided by peak position map T = 1.2 K
KPFM maps	62±14 (185)	present work	averaging effects lead to underestimation T = 1.2 K
DFT	130	[51]	Moiré
DFT	90	[32, 51]	1 × 1

3.3 Discussion

STM based Φ variation measurements can detect lateral Φ variations at the scale of a few nm. For the case of *h*-BN/Cu(111) where the Φ varies on that order radiation-based techniques suffer from averaging over large structures and can't provide later Φ variation information which is of central importance to study adsorbed species, e.g., molecules in trapped potentials at valleys. The high resolution Φ measurement done using FER maps [80, 84, 90] provides a Φ variation between rim and valley to be 143±11 meV which is in close agreement to the DFT calculations [32, 51]. Using 24×24 *h*-BN overlaid on 23×23 4-layer Cu(111) slab with certain rotation angle, to generate Moiré superstructure, is topographically planar with small changes in adsorption registry. Φ variation between regions where BN is adsorbed in $\mathrm{B}_{fcc}\mathrm{N}_{top}$ and $\mathrm{B}_{hcp}\mathrm{N}_{fcc}$ configuration is 130 meV as shown in Table 3.1. Using 1×1 adsorption a Φ variation of 90 meV between the two extreme cases was calculated.

The approach curve measurement provides a Φ variation of 300 meV [51]. This measurement suffers from significant errors due to diagonal movement of the tip during approach. Since the value is calculated just by single measurements at rim and valley site, it does not provide a good estimate of the overall Φ variation. For the KPFM measurement, the weighted-averaging over the size of the tip means that small-scale variations are averaged over and for the case of *h*-BN/Cu(111). Thus, the measurement underestimates Φ variation to the value of 62±14 meV. The discrepancies between calculated and measured values can be explained by the uncertainty in the exact position of B and N atoms over the Cu(111) slab. For such a loosely bound decoupling layer the dispersion forces involved cannot be exactly accounted for using DFT calculations, and thus, experimental measurement of Φ variations becomes important [18]. Φ variation measured using the shift in the peak position of the first FER state provided a highly resolved, accurate work function variation for the system.

Chapter 4

Stiffness of *h*-BN/Cu(111)

This chapter provides an insight into our investigation of the stiffness of an *h*-BN monolayer on Cu(111). In a previous study on *h*-BN/Rh(111) [41] lateral and vertical stiffness were quantified. On the weakly bound rim regions of *h*-BN, the vertical stiffness obtained in this experiment were similar to the ones for BN sheet using indentation experiments [3]. In our experiment on *h*-BN/Cu(111) however, even though lateral and vertical deformation was evident, quantification of lateral stiffness was not possible. The experimental procedure for such a measurement and data treatment is elaborated upon in the following. Vertical stiffness in the repulsive and attractive regime is discussed. A preliminary analysis shows that *h*-BN/Cu(111) is stiffer than *h*-BN/Rh(111) which is expected due to comparatively less corrugation in the former [41].

4.1 Data acquisition and treatment

To obtain spatial information in all three dimensions 3D Force maps of the area of interest were taken. The combined STM/AFM functionality of our instrument lets us measure frequency shift, Δf and the electrical conductance, $G = I/V$, between the tip and sample. Exponential dependence of G allows for the determination of absolute tip-sample separation and low oscillation amplitude (50 pm) during the measurement allows detection of minute variations in the corrugation.

To prepare for the acquisition of aforementioned force maps the following procedure was followed. Firstly, a large, defect-free patch of the *h*-BN/Cu(111) surface was located, and the tilt correction function was used to compensate for the tilt. Following this, a patch of 10×10 nm^2 with a few valley-rim areas was selected. This is the same area, the one used for FER and KPFM measurements. Therefore, the z-piezo creep is minimal due to long waiting time. The scanning mode is then switched to the constant height mode, and the bias voltage is lowered to 0 V. At last, the tip is approached

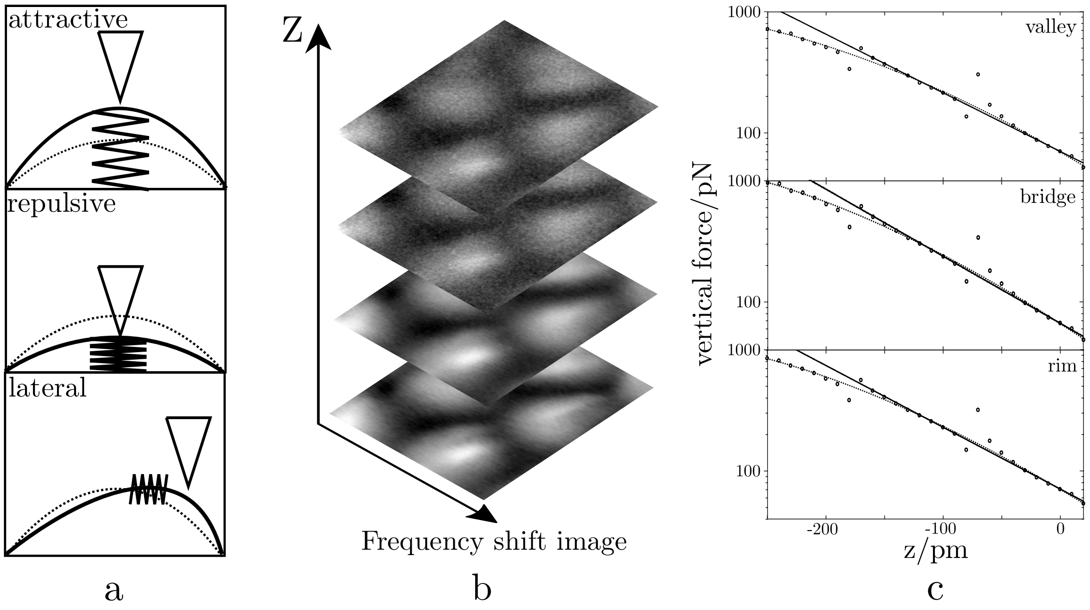

Fig. 4.1 Stiffness of *h*-BN/Cu(111). a. Schematic of effective stiffness probed in case of vertical attractive, vertical repulsive and lateral attractive forces [40]. b. Selected frequency shift images from a set of constant height measurement. Only the superstructure is resolved in these images. c. Semi-log plot of the averaged vertical force over bridge, rim and valley areas. Exponential fit in x-range: -180-20 pm is shown. Dotted line acts as a guide to eye for spotting possible over-exponential behavior.

-250 pm using the Z-controller module. A LabView script controls the data acquisition. Since the constant height mode required slow scanning speed, to optimize acquisition time, it was decided to take 128×128-pixel images. After each image, the script retracts the tip by 10 pm and starts a new scan. The tip was retracted until the contrast between rim and valley regions is lost. For the particular measurement presented here, the starting set point of I = 100 pA, V_{bias} = 10 mV was chosen. After the tip had been retracted from -250 pm to +20 pm (27 images) the contrast between rim and valley was minimal. Four frequency shift images indicating changes in corrugation for certain approach distances are shown in Fig. 4.1. These images can be seen as 128×128 pixel discrete frequency shift approach curves. For FM-AFM, force is not directly proportional to frequency shift, but instead to the average force gradient (see Eq. 1.31) [62]. To deconvolve the force from our frequency shift data we used the so-called matrix method proposed by Giessibl [30]. The Eq. 1.31 is discretized, by appropriate substitution and index shifting, and rewritten as

$$\Delta f_i = \sum_{j=1}^{N} W_{ij} F_j \tag{4.1}$$

where Δf_i represents discrete, equidistant frequency shift data points. F is the arbitrary force between tip and sample. The matrix elements, W_{ij} represent integral terms used in the derivation of frequency shift caused by an arbitrary force using Hamilton-Jacobi formalism [27]. Multiplying Eq. 4.1 from left by inverse matrix $M = W^{-1}$ gives

$$\Delta F_j = \sum_{i=1}^{N} M_{ji} \Delta f_i \tag{4.2}$$

Thus, the deconvolution method does not depend on any approximation (like Sader-Jarvis method [78]) and only involves calculating inverse matrix M.

In Fig. 4.1, a schematic explaining the measurement principle of this measurement is presented. The dotted line represents the rim region of *h*-BN/Cu(111). When the tip is far away from the surface, there is no interaction between the two. As the tip approaches, attractive short-range forces come into play, and for a soft corrugated *h*-BN layer it's expected that it gets pulled up towards the tip. Fig. 4.1(a) shows the said situation. If the tip is approached further in, the short-range interactions (Pauli-repulsion) come into play, and the adlayer gets pushed in. If the tip scans over the strained rim area, one could compare the shift in atomic positions to a less strained case and get the lateral stiffness parameters. This case requires an unprecedented atomic resolution which can be extremely hard to achieve. For the presented measurement atomic resolution could not be achieved and thus, for the time being, a lateral stiffness calculation has been skipped. The next section provides insight into first measurements and preliminary analysis of the vertical stiffness part.

4.2 Vertical forces

Depending on the stiffness of the decoupling layer, the tip affects the corrugation normal to the surface. We observe no deformation in the range between -250 pm and 20 pm of the set point (see Fig. 4.1(b)). Semi-log plots of the vertical force against approach distance for the valley, bridge, and rim areas is shown in Fig. 4.1(c). In this z-range, only the attractive part of the Morse-type force is seen. Though the last data points do indicate a transition into the repulsive regime. In this section, a preliminary analysis of attractive force and first indications from it are presented.

In Fig. 4.1(c) an exponential fit to the data with z between -180 and 20 pm is shown. The range from -250- -180 pm has hint of an under-exponential behavior. The dotted line acts as a guide to the eye to follow the said behavior. This observation may stem from the repulsive interactions in play in this z-range. The decay constant (-9.55 nm^{-1}) is strikingly close for all the regions indicating that rim and valley region

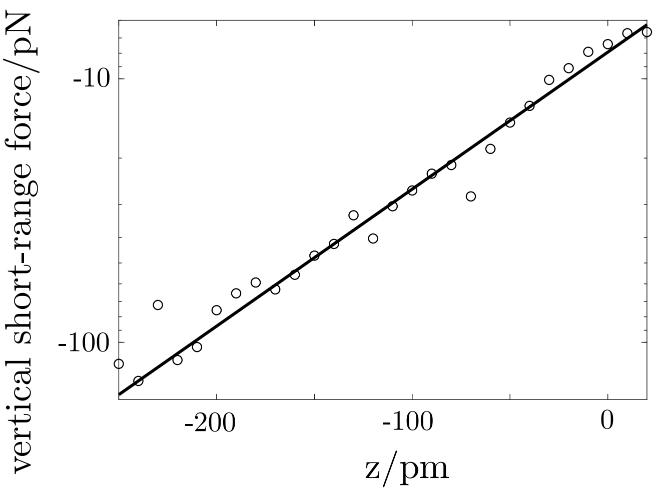

Fig. 4.2 Semi-log plot of short-range contribution from overall force data against z-approach adn its exponential fit.

undergo similar deformation if any. On a closer look, one finds that slightly higher forces are involved for rim and bridge, as compared to the valley. This observation leads one to question the flatness of *h*-BN/Cu(111). To analyze it further one can have a look at the short-range forces involved at rim region.

Presuming that the forces involved in valley area are long range in nature, one can subtract them from forces at the rim area to calculate the short-range contribution. The force averaged over valley area is subtracted from the one obtained for rim area to obtain the magnitude of short-range forces. In Fig. 4.2 a semi-log plot of the force against z-approach is shown. Exponential fit (decay constant: 10.3 nm^{-1}) of the data shows no over exponential (keep in mind the small z-range) behavior. This observation seconds our previous claim of no deformation being seen for the valley and rim areas on *h*-BN/Cu(111). No deformation of the layer indicates higher stiffness of the system, e.g., as compared to *h*-BN/Rh(111) [40, 41].

4.3 Discussion

There has been a long-standing debate on the flatness of *h*-BN/Cu(111) since the first claim of the corrugation being purely electronic [51]. Recent measurements claim a minor corrugation between hill and valley region of 0.3-0.45 Å [81]. The measurements provided in the chapter cannot detect the corrugation difference between the two areas but offer an intuitive way of observing any effect of such corrugation.

The 3D stiffness measurement of a quasi-2D (debated) strained layer shows no difference in forces involved at rim and valley area. This indicates minute corrugation in *h*-BN/Cu(111) if any. The short-range force contribution at rim area that showed over exponential behavior for *h*-BN/Rh(111) shows an exponential behavior for this system. Thus, no deformation at any of the sites in the layer is observed indicating that the layer is quite stiff. The possibility of various rotations of the adlayer leading to Moiré superstructures also suggests that layer is not as strongly coupled to the metal surface as *h*-BN/Rh(111) [40, 41]. Further stiffness measurement with larger approach range could provide more insight into the stiffness of layer in all dimensions. With the new insight may be a more informed comment on flatness can be made.

Chapter 5

Co and CoH$_x$ on *h*-BN/Cu(111)

The suggested flatness of *h*-BN/Cu(111) motivated us to choose this system for extending our study of the Kondo effect using magnetic adatoms. Following the electronic and structural characterization of the decoupling layer single cobalt atoms were deposited on the surface. The following presents an overview of the first results in the context of the Kondo effect in this system. Firstly, a brief theoretical model of the Kondo effect is discussed for the spin-1/2 case. Secondly, spectroscopic features obtained on possibly different Co species are presented.

5.1 Kondo effect

For a normal metal, the resistance drops with decreasing temperature, and saturates below ~10 K, reaching a value that depends on the concentration of defects in the metal. However, already in the 1930s, experiments showed that the resistance of a gold sample with iron impurities was found to decrease with temperature up to a minimum value, but for even lower temperatures it started to increase again [16]. Jun Kondo came forward with a model to explain this unique behavior of electrical resistance [53]. He associated this anomalous increase in the resistivity with the presence of magnetic impurities in the metal and the consequent formation of a resonant state at the Fermi energy. This happens below a characteristic temperature, the Kondo temperature, T$_K$, that depends on the coupling strength between the impurity and the electron bath [42].

He explained the process as a many-body interaction between a single magnetic atom and the many electrons in a non-magnetic metal. In the most straightforward picture (Anderson impurity model [1]), the magnetic impurity has only one electron that can be exchanged with the bath via a virtual process [92]. The minimum energy configuration corresponds to the formation of a spin singlet (the Kondo state) between the localized moment and the net spin of the electron bath that screens the spin of the

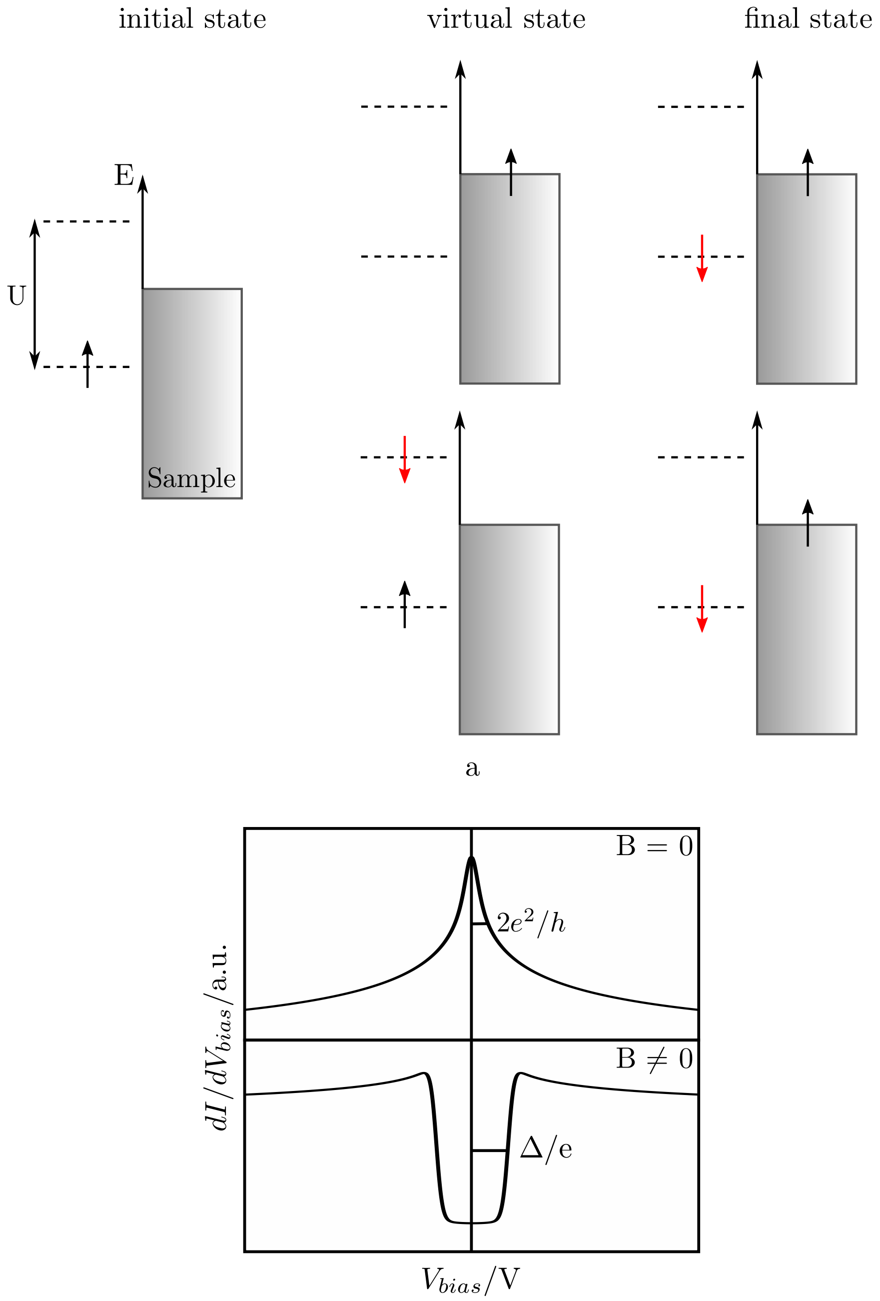

a

b

Fig. 5.1 The Kondo effect. a. Schematic of a general inelastic co-tunneling process. In the initial configuration, the magnetic atom is in the ground state; in the final configuration, one spin has been flipped. This can happen in two possible virtual ways: a hole or an electron can tunnel to the magnetic atom without conserving the energy, and at the same time another hole or electron can tunnel from the magnetic atom to the other side of the barrier. In this way, the system has changed its magnetization. b. Schematic of differential conductance dI/dV_{bias} through a single Kondo impurity as a function of bias voltage V_{bias}. In the case of two levels shown in (a), split by an energy Δ (bottom), an inelastic transport channel opens up when the bias exceeds Δ/e. When the splitting between levels is reduced to zero (top), as for a spin-1/2 impurity in zero magnetic fields, the logarithmically diverging peak in dI/dV_{bias} persists at zero bias (top). This is the perturbative signature of the Kondo effect.

magnetic impurity. As a result, a sharp resonance peak appears in the electron density of states at the Fermi energy.

The peak structure obtained for Kondo resonance in STM measurements can be explained using the perturbation approach based on the Anderson model. The increase in tunneling probability can be explained by taking interferences among different order contributions into account [92]. Summing over all transition intensities and integrating over the energy bandwidth, ω_0, of the substrate electrons with the spin system leads the observable differential conductance in STM experiments to be

$$\frac{dI}{dV} \propto \rho_{sample}(\varepsilon_F) \int_{-\omega_0}^{\omega_0} \frac{g(\varepsilon)}{\varepsilon} d\varepsilon \tag{5.1}$$

where integration of $1/\varepsilon$ leads to the logarithmic line-shape of Kondo resonance.

This approach only explains the scenario where higher order terms can be neglected [92]. The characteristic temperature (Kondo temperature) at which the breakdown of this approach happens is

$$T_K = \frac{\Gamma}{k_B} \tag{5.2}$$

where Γ is the HWHM of the Kondo resonance at 0 K.

When a magnetic atom is deposited directly on top of metal the interactions with the conduction electrons are very strong, giving rise to a Kondo temperature in the order of 30-100 K [52, 96]. The Kondo interaction, and as a consequence T_K, is reduced if there is a decoupling layer like h-BN or Cu_2N separating the magnetic atom from the bulk substrate [46, 47, 64, 67]. For example, for Co atoms on Cu_2N, the Kondo temperature is found to be T_K = 2.6 ± 0.2 K [68]. For Co on h-BN/Rh(111), T_K is found to be around the same temperature, which is also the base temperature of our instrument [40, 97].

The pre-requisite for a spin to be Kondo screened is the ability of a single electron from the bath to flip it. Therefore, its ground state needs to fulfill certain criteria: it needs to be at least twofold degenerate, and the magnetization m of two degenerate ground states needs to differ by $|\Delta m|$ = 1. Co ($S = 3/2$) is an ideal candidate for Kondo screening [58].

Another issue that comes while analyzing the Kondo resonance is its varying, asymmetric structure on metal substrates. This interference can be falsely interpreted as a dip or step-like feature [12, 59, 92]. The interference between the two tunneling pathways, i.e., the scattering tip and magnetic impurity and the generic tip-sample tunneling. Such cases may be described by a Fano line-shape

$$\frac{dI}{dV} \propto \frac{(q+\varepsilon)^2}{(1+\varepsilon^2)} \tag{5.3}$$

where $\varepsilon = (eV - \varepsilon_K)/k_BT_K$, q and ε_K are the asymmetry parameter and the energy position of the resonance respectively [23, 92]. This gives FWHM of the resonance to be $2k_BT_K$. Fano line-shape includes the interference between a Lorentzian and the constant part of Kondo resonance [23]. A varying Fano parameter can explain both the dip and peak-like structures that are sometimes obtained for such measurements [12, 59, 92]. In the present work, these Kondo resonances are fitted to a Frota line-shape [25]. The following formula

$$D(\varepsilon) = \frac{2}{\pi\Gamma_A} \operatorname{Re}\left[\frac{\imath\Gamma_K}{\varepsilon + \imath\Gamma_K}\right]^{1/2} \tag{5.4}$$

where Γ_A is given by Friedel sum rule for intensity of the resonance, accurately describes the Kondo resonance.

5.2 Overview of Kondo features observed

This section provides an overview of the various spectroscopic features measured on CoH_x adsorbates on *h*-BN/Cu(111). On our first evaporation of Co, the adsorbates were found to be mobile and could not be scanned easily. The influence of the tip seemed to be enough to push the atoms away from the scanning area. Later, on a partially covered surface with an evaporation time of 60 s, a low coverage of Co on *h*-BN/Cu(111) was obtained. All the measurements presented in this section were taken on the sample mentioned above. In Fig. 5.2(a), a pseudo 3D image generated from constant current STM image is shown. *h*-BN growing over the copper terraces can be seen with a bare Cu(111) patch in the middle. Co adsorbates have an apparent height of ~200 pm on *h*-BN/Cu(111) and ~100 pm on Cu(111) (Set point: 100 pA, -50 mV).

To elaborate upon why CoH_x complexes are obtained along with single Co atoms it's important to mention that the Co evaporator is more than one meter away from the sample surface. This translates into requiring high Co flux even for a fraction of the sub-monolayer coverage [40]. This led us to believe that residual H from the chamber gets co-deposited leading to formation of CoH_x complexes. During the experiments on Co on *h*-BN/Rh(111) the same issue was addressed by careful outgassing, but it does not seem to completely avoid hydrogen contamination [47, 63]. Anyhow, the variety of CoH species offer an exciting playground with their varying spin signatures [46, 64].

A general set of spectroscopic features obtained from Co on *h*-BN/Cu(111) is shown in 5.2(b). Two variants of the characteristic zero-bias peak for spin-1/2 species are observed on ~20% of the adsorbates. Close to ~80% of these were the broad Kondo

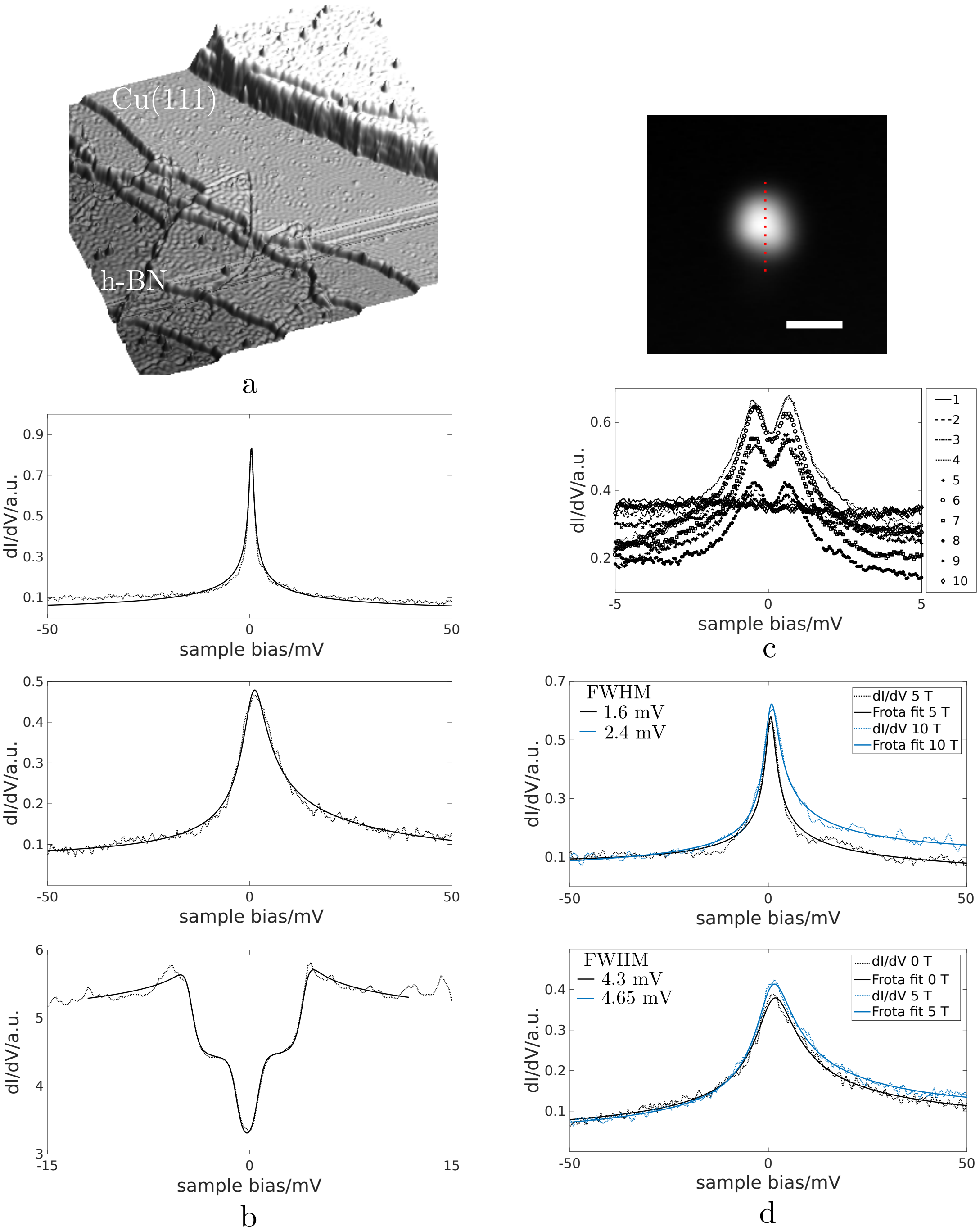

a

c

b

d

Fig. 5.2 Kondo features of presumably different CoH$_x$ species on *h*-BN/Cu(111) . a. Pseudo 3D image of *h*-BN/Cu(111) after Co evaporation (100×100 nm^2). CoH$_x$ adsorbates can be identified using their apparent height (~200 pm) and size (1×1 nm^2). b. Sharp and broad spin-1/2 Kondo signature observed on *h*-BN/Cu(111). On some rare occasions (<1%) spin-1 signatures were observed (bottom spectrum). c. Kondo signatures under B-field. Zeeman energy splitting of the Kondo peak at B = 5 T. $\Delta\Gamma \approx 800$ μeV was observed which corresponds approximately to the magnetic energy for B = 5 T (578 μeV for $g = 2$). Scale bar: 1 nm. d. No splitting of sharp Kondo peak at B = 5 and 10 T. Sharp and broad are broadened by the magnetic field energy but do not exhibit any splitting.

feature shown in the center frame in Fig. 5.2(b). FWHM for such features ranged from 4-15 meV with a signal to background ratio of 300-500%. These peaks were successfully fit using Fano line-shapes (Eq. 5.3). The sharp features, shown in Fig. 5.2(b) have FWHM ranging from 0.8-3 meV with signal to background ratio of over 700%. Frota line shape was used to fit both the peak features and the FWHM reported are obtained from it. For some extremely sharp features the Frota line-shape could not successfully fit the height of the peak (see Fig. 5.2(b)). In some extremely rare cases, we obtained spin-1 features which have magnetic anisotropies similar to the ones obtained on *h*-BN/Rh(111) [64].

One way to verify these spectroscopic features being related to the Kondo effect is by looking at them in a magnetic field. Fig. 5.2(c) shows splitting in one of the sharp features. The red dotted line corresponds to the measurement position of dI/dV on the atom. It can be seen that the split peak is observed as the measurement position travels over the center of the atom and fades slowly as it surpasses it. Surprisingly, not all the sharp Kondo-related features were split at a high magnetic field of 5 and 10 T. For the broad features, only an energy broadening is expected as the Zeeman energy at the magnetic field is not high enough to split them (see Fig. 5.2(d)). The robustness of the sharp Kondo feature is interesting, and further investigation is required to get a deeper insight.

The sharpness of the Kondo features could be related to the adsorption site. Even though *h*-BN/Cu(111) is not as corrugated as *h*-BN/Rh(111) the observation that $\mathrm{CoH_x}$ species did not always show a spectroscopic feature at the valley sites could be extrapolated to the present case. However, it's not that straightforward to determine the adsorption site for *h*-BN/Cu(111). As mentioned before, the high bias voltages required to observe the contrast between rim and valley sites are not suitable to scan over highly mobile $\mathrm{CoH_x}$ adsorbates.

Another interesting observation related to the Kondo features that did not split is the development of an asymmetry between negative and positive bias. For the cases of both sharp and broad Kondo feature, the broadening of peak occurred in the positive bias leading to the said asymmetry. It was verified by doing background dI/dV measurement that this feature did not originate from the tip which showed a flat density of states for this energy range.

5.3 Discussion

$\mathrm{CoH_x}$ on *h*-BN/Cu(111) is an interesting playground to study manifestations of the Kondo effect [56, 70, 83]. Not only for different spectroscopic features due to the chemically different species, but also due to the adsorption of the same species at slightly different sites. The spectroscopic features obtained for $\mathrm{CoH_x}$ were addressed in two categories: sharp and broad, concerning their FWHM. The sharp peaks had FWHM ranging from 0.5-3 meV and the broad ones from 3-15 meV. Roughly 20% of all adsorbates showed Kondo resonance at Fermi energy, and more than 80% of them were broad ones. In magnetic field, B = 5T, energy splitting of $\approx$ 800 µeV was obtained for the sharp peak. Surprisingly, most of the sharp peaks did not show any splitting in the magnetic field up to 10 T. The broad peak features underwent broadening as the Zeeman energy is not high enough to split these peaks. The possible reason for a variety of features obtained could be different adsorption sites on the *h*-BN (i.e., N, B, or hollow site). Also, the H concentration in the $\mathrm{CoH_x}$ specie could lead to these features. Further investigation is required to deconvolve the effect of adsorption sites on the Kondo effect of $\mathrm{CoH_x}$ on *h*-BN/Cu(111).

The next steps involve using the combined STM/AFM functionality of our instrument for determination of the adsorption sites of the adsorbates concerning a valley and rim areas using the fact that the contrast can still be observed at low bias voltages in the frequency shift channel. It was also observed that adsorbates stuck to the tip when it scanned over the surface at positive bias voltages of around 100 meV. Pulsing did to clean the tip (at a negative bias voltage of 10 V) led to the adsorbates being found on the previously clean *h*-BN/Cu(111) areas. This approach, however, is not very reliable as a variety of adsorbates are obtained on the surface which shows a range of spectroscopic features. Vertical manipulation of adsorbates did not seem so straightforward with the Pt tip we use as the magnetic atom has much more affinity towards the metal than the decoupling layer. Also, better control over H contamination would go a long way in lifting discrepancy over the variety of features observed.

Chapter 6

Summary and Outlook

The work presented in this thesis, for the most part, involved preliminary structural and electronic characterization of the *h*-BN/Cu(111) substrate using a low temperature combined STM/AFM. The studies of the Kondo effect on CoH_x species revealed the non-triviality of the analysis of such spectroscopic features on corrugated decoupling layers like *h*-BN. Nevertheless, CoH_x on *h*-BN/Cu(111) provides a vibrant playing field for manifestations of Kondo interactions depending on the coupling between the magnetic impurity and the electron bath.

The tip-sample approach is optimized, as discussed in Chapter 2, using a kink in the junction capaceitance at a low tip-sample distance (~1 µm) as the cut-off criteria for switching from coarse to auto approach. This optimization has saved us precious measurement time. This method can be easily extrapolated to other scanning probe-based instruments [79]. The idea of de Voogd *et al.* to follow the capacitance change during the approach to optimize approach mechanism relies on the same physical principles [17]. However, the presented method is a bit more conservative, arguably safer way to switch from coarse to auto approach, which is closer to the conventional approach mechanism.

In Chapter 3, the Φ variations on *h*-BN/Cu(111) are discussed. The corrugation observed was pinned entirely on the electronic structure and *h*-BN itself was presumed to be flat in the first report on this surface [32, 51]. However, recently it was updated that a minimal corrugation of 0.45 Å is present between the valley and rim regions with a height of *h*-BN over Cu(111) around 3.38 ± 0.06 Å [81]. In our case, the Φ variation corresponds to the electronic corrugation of the layer. The value of the first FER shift is found to be 143 ± 11 meV. This value is in agreement with the value predicted by DFT [32, 51]. The complimentary measurement using KPFM underestimates the magnitude of Φ variation due to the averaging effects stemming from the averaging over tip dimensions. FER provide a high-resolution map of such variations on the surface. The trapping of resonances in the valley led to ring-like structures inside the valley at specific energies. A model in the context of modes existing in circular potential well states could shed some light onto this observation.

From the preliminary analysis of the vertical stiffness measurement on the monolayer, one could infer that *h*-BN/Cu(111) is much stiffer than *h*-BN/Rh(111) as the rim, bridge and valley areas undergo similar changes under the tip influence during the constant height frequency shift maps. An analysis of vertical short-range forces for the rim area showed no deformation of the layer which reflects its higher stiffness than *h*-BN/Rh(111) [40, 41]. Nevertheless, this measurement with its dependency on precision and stability due to long measurement time is an excellent representation of the stability of our instrument.

The first measurements of magnetic impurities on *h*-BN/Cu(111) were reported. CoH_x species showed a range of spectroscopic features which are still not completely understood. As discussed in Chapter 5, both the chemical nature and the adsorption site of the species could lead to the variety of features. However, the measurements in different magnetic fields prove the origin of these signatures to be due to the Kondo effect. The sharp peak showed a splitting of ~800 μeV at $B = 5$ T. Surprisingly, the majority of the peaks, both sharp and broad, only underwent broadening and a development of an asymmetry. Further investigation using nc-AFM scanning could shed light onto the adsorption site of these species and hence, pinpoint the origin of the various features observed.

Outlook

Decoupling layers such as *h*-BN/Cu(111) provide an interesting template for confining adsorbed molecules or other species in electronic potential traps [50]. This provides an interesting alternative approach to nano-patterning on the surface. Another aspect of the *h*-BN layer is that controlled defects could enhance its capacity to trap and immobilize adsorbates, while still conserving their magnetic and electronic properties [10]. Periodic arrays of immobilized adsorbates can even lead to the emergence of new electrical, magnetic and optical properties [44, 99], potentially making it a multi-functional coating.

The Kondo effect depends highly on the coupling strength along with the modulation of magnetic anisotropy energies of magnetic atoms due to local fields. Systems like Co on Cu_2N, Rh(111) or Cu(100) [52, 58, 64, 96] were already used to display Kondo exchange dependency on relative adsorption sites. Even though *h*-BN/Rh(111) served as a great passivity layer, it suffered from a strong corrugation leading to local strains in the layer affecting the Kondo exchange [46, 47, 64]. *h*-BN/Cu(111) which was prophesied to be flat with only an electronic corrugation, shows slight mechanical corrugation from the preliminary analysis. This hinders one from pin-pointing at the exact influence of conduction electrons from the substrate or the local strain or defects. The determination and control of the coupling of spin systems to a metal electrode is a topic that is not only interesting for a general scientific understanding but also provides application guidelines for the design of atomic qubits that could mediate and control the qubits' decoherence with the environment.

References

[1] Anderson, P. W. (1961). Localized Magnetic States in Metals. *Physical Review*, 124:41–53.

[2] Bardeen, J. (1961). Tunnelling from a many-particle point of view. *Phys. Rev. Lett.*, 6:57–59.

[3] Bhatia, N. (1968). Finite indentation of an elastic membrane by a spherical indenter. *International Journal of Non Linear Mechanics*, 3:307–324.

[4] Binnig, G., Garcia, N., and Rohrer, H. (1985). Conductivity sensitivity of inelastic scanning tunneling microscopy. *Phys. Rev. B*, 32:1336–1338.

[5] Binnig, G., Quate, C. F., and Gerber, C. (1986). Atomic force microscope. *Phys Rev Lett*, 56(9):930–933.

[6] Binnig, G., Rohrer, H., Gerber, C., and Weibel, E. (1982a). Surface studies by scanning tunneling microscopy. *Phys. Rev. Lett.*, 49:57–61.

[7] Binnig, G., Rohrer, H., Gerber, C., and Weibel, E. (1982b). Tunneling through a controllable vacuum gap. *Applied Physics Letters*, 40(2):178–180.

[8] Borca, B., Barja, S., Garnica, M., Sánchez-Portal, D., Silkin, V. M., Chulkov, E. V., Hermanns, C. F., Hinarejos, J. J., Vázquez de Parga, A. L., Arnau, A., Echenique, P. M., and Miranda, R. (2010). Potential energy landscape for hot electrons in periodically nanostructured graphene. *Phys. Rev. Lett.*, 105:036804.

[9] Bradley, A. J. (2015). *Local Probe Investigation of the Electronic Structure of Molecule–Based and Transition–Metal–Based Low Dimensional Systems Using Cryogenic Scanning Tunneling Microscopy and Spectroscopy*. PhD thesis, University of California, Berkeley.

[10] Brihuega, I., Michaelis, C. H., Zhang, J., Bose, S., Sessi, V., Honolka, J., Alexander Schneider, M., Enders, A., and Kern, K. (2008). Electronic decoupling and templating of Co nanocluster arrays on the boron nitride nanomesh. *Surface Science*, 602:L95–L99.

[11] Chen, C. J. (2007). *Introduction to Scanning Tunneling Microscopy*. Oxford Scholarship Online.

[12] Choi, D.-J., Rastei, M. V., Simon, P., and Limot, L. (2012). Conductance-driven change of the kondo effect in a single cobalt atom. *Phys. Rev. Lett.*, 108:266803.

[13] Crampin, S. (2005). Lifetimes of Stark-Shifted Image States. *Physical Review Letters*, 95(4):046801.

[14] Crommie, M. F., Lutz, C. P., and Eigler, D. M. (1993). Confinement of electrons to quantum corrals on a metal surface. *Science*, 262(5131):218–20.

[15] Davey, W. P. (1925). Precision Measurements of the Lattice Constants of Twelve Common Metals. *Physical Review*, 25:753–761.

[16] De Haas, W. J. and Van Den Berg, G. J. (1936). The electrical resistance of gold and silver at low temperatures. *Physica*, 3:440–449.

[17] de Voogd, J. M., van Spronsen, M. A., Kalff, F. E., Bryant, B., Ostojić, O., den Haan, A. M. J., Groot, I. M. N., Oosterkamp, T. H., Otte, A. F., and Rost, M. J. (2017). Fast and reliable pre-approach for scanning probe microscopes based on tip-sample capacitance. *Ultramicroscopy*, 181:61–69.

[18] Dil, H., Lobo-Checa, J., Laskowski, R., Blaha, P., Berner, S., Osterwalder, J., and Greber, T. (2008). Surface trapping of atoms and molecules with dipole rings. *Science*, 319(5871):1824–1826.

[19] Dirac, P. A. M. (1927). The Quantum Theory of the Emission and Absorption of Radiation. *Proceedings of the Royal Society of London Series A*, 114:243–265.

[20] Dong, G., Fourré, E. B., Tabak, F. C., and Frenken, J. W. M. (2010). How Boron Nitride Forms a Regular Nanomesh on Rh(111). *Physical Review Letters*, 104(9):096102.

[21] Dutton, G., Pu, J., Truhlar, D. G., and Zhu, X.-Y. (2003). Lateral confinement of image electron wave function by an interfacial dipole lattice. *The Journal of Chemical Physics*, 118:4337–4340.

[22] Echenique, P. M. and Uranga, M. E. (1991). Image potential states at surfaces. *Surface Science*, 247:125–132.

[23] Fano, U. (1961). Effects of configuration interaction on intensities and phase shifts. *Phys. Rev.*, 124:1866–1878.

[24] Feuchtwang, T. E., Cutler, P. H., and Miskovsky, N. M. (1983). A theory of vacuum tunneling microscopy. *Physics Letters A*, 99:167–171.

[25] Frota, H. O. (1992). Shape of the kondo resonance. *Phys. Rev. B*, 45:1096–1099.

[26] Giessibl, F. J. (1995). Atomic force microscopy-(7x7) surface by atomic force microscopy. *Science*, 267(5194):68–71.

[27] Giessibl, F. J. (1997). Forces and frequency shifts in atomic-resolution dynamic-force microscopy. *Phys. Rev. B*, 56:16010–16015.

[28] Giessibl, F. J. (1998). High-speed force sensor for force microscopy and profilometry utilizing a quartz tuning fork. *Applied Physics Letters*, 73(26):3956–3958.

[29] Giessibl, F. J. (2000). Atomic resolution on si(111)-(7×7) by noncontact atomic force microscopy with a force sensor based on a quartz tuning fork. *Applied Physics Letters*, 76(11):1470–1472.

[30] Giessibl, F. J. (2001). A direct method to calculate tip–sample forces from frequency shifts in frequency-modulation atomic force microscopy. *Applied Physics Letters*, 78(1):123–125.

[31] Gimzewski, J. K. and Joachim, C. (1999). Nanoscale science of single molecules using local probes. *Science*, 283(5408):1683–8.

[32] Gómez Díaz, J., Ding, Y., Koitz, R., Seitsonen, A. P., Iannuzzi, M., and Hutter, J. (2013). Hexagonal boron nitride on transition metal surfaces. *Theoretical Chemistry Accounts*, 132(4):1350.

[33] Gottlieb, A. D. and Wesoloski, L. (2006). Bardeen's tunnelling theory as applied to scanning tunnelling microscopy: a technical guide to the traditional interpretation. *Nanotechnology*, 17(8):R57.

[34] Griffiths, D. J. (2016). *Introduction to Quantum Mechanics*. Cambridge University Press, 2016.

[35] Gundlach, K. H. (1966). Zur berechnung des tunnelstroms durch eine trapezförmige potentialstufe. *Solid State Electronics*, 9:949–957.

[36] Harrison, W. A. (1980). *Solid State Theory*. Dover Publications, Inc.

[37] Heinrich, A. J., Gupta, J. A., Lutz, C. P., and Eigler, D. M. (2004). Single-atom spin-flip spectroscopy. *Science*, 306(5695):466–9.

[38] Heinrich, A. J., Lutz, C. P., Gupta, J. A., and Eigler, D. M. (2002). Molecule cascades. *Science*, 298(5597):1381–7.

[39] Herden, T. (2010). Aufbau eines q-sensor afm/stms für den einsatz bei tiefen temperaturen.

[40] Herden, T. (2014). *Combined Scanning Tunneling and Atomic Force Microscopy and Spectroscopy on Molecular Nanostructures*. PhD thesis, Universität Konstanz, Konstanz.

[41] Herden, T., Ternes, M., and Kern, K. (2014). Lateral and vertical stiffness of the epitaxial h-bn monolayer on rh(111). *Nano Lett*, 14(6):3623–7.

[42] Hewson, A. C. (1997). *The Kondo Problem to Heavy Fermions*.

[43] Hirjibehedin, C. F., Lin, C.-Y., Otte, A. F., Ternes, M., Lutz, C. P., Jones, B. A., and Heinrich, A. J. (2007a). Large magnetic anisotropy of a single atomic spin embedded in a surface molecular network. *Science*, 317(5842):1199–1203.

[44] Hirjibehedin, C. F., Lin, C. Y., Otte, A. F., Ternes, M., Lutz, C. P., Jones, B. A., and Heinrich, A. J. (2007b). Large magnetic anisotropy of a single atomic spin embedded in a surface molecular network. *Science*, 317(5842):1199–203.

[45] Ho, W. (2002). Single-molecule chemistry. *The Journal of Chemical Physics*, 117(24):11033–11061.

[46] Jacobson, P., Herden, T., Muenks, M., Laskin, G., Brovko, O., Stepanyuk, V., Ternes, M., and Kern, K. (2015). Quantum engineering of spin and anisotropy in magnetic molecular junctions. *Nat Commun*, 6:8536.

[47] Jacobson, P., Muenks, M., Laskin, G., Brovko, O., Stepanyuk, V., Ternes, M., and Kern, K. (2017). Potential energy-driven spin manipulation via a controllable hydrogen ligand. *Sci Adv*, 3(4):e1602060.

[48] Jaklevic, R. C. and Lambe, J. (1966). Molecular vibration spectra by electron tunneling. *Phys. Rev. Lett.*, 17:1139–1140.

[49] Joachim, C., Gimzewski, J. K., and Aviram, A. (2000). Electronics using hybrid-molecular and mono-molecular devices. *Nature*, 408(6812):541–8.

[50] Joshi, S., Bischoff, F., Koitz, R., Ecija, D., Seufert, K., Seitsonen, A. P., Hutter, J., Diller, K., Urgel, J. I., Sachdev, H., Barth, J. V., and Auwärter, W. (2013). Control of molecular organization and energy level alignment by an electronically nanopatterned boron nitride template. *ACS Nano*, 8(1):430–442.

[51] Joshi, S., Ecija, D., Koitz, R., Iannuzzi, M., Seitsonen, A. P., Hutter, J., Sachdev, H., Vijayaraghavan, S., Bischoff, F., Seufert, K., Barth, J. V., and Auwärter, W. (2012). Boron nitride on cu(111): an electronically corrugated monolayer. *Nano Lett*, 12(11):5821–8.

[52] Knorr, N., Schneider, M. A., Diekhöner, L., Wahl, P., and Kern, K. (2002). Kondo Effect of Single Co Adatoms on Cu Surfaces. *Physical Review Letters*, 88(9):096804.

[53] Kondo, J. (1964). Resistance Minimum in Dilute Magnetic Alloys. *Progress of Theoretical Physics*, 32:37–49.

[54] Kröger, J., Limot, L., Jensen, H., Berndt, R., and Johansson, P. (2004). Stark effect in Au(111) and Cu(111) surface states. *Phys. Rev. B*, 70:033401.

[55] Lang, N. D. (1986). Spectroscopy of single atoms in the scanning tunneling microscope. *Phys. Rev. B*, 34:5947–5950.

[56] Liang, W., Shores, M. P., Bockrath, M., Long, J. R., and Park, H. (2002). Kondo resonance in a single-molecule transistor. *Nature*, 417:725–729.

[57] Limot, L., Maroutian, T., Johansson, P., and Berndt, R. (2003). Surface-state stark shift in a scanning tunneling microscope. *Phys. Rev. Lett.*, 91:196801.

[58] Madhavan, V., Chen, W., Jamneala, T., Crommie, M. F., and Wingreen, N. S. (1998). Tunneling into a Single Magnetic Atom: Spectroscopic Evidence of the Kondo Resonance. *Science*, 280:567.

[59] Manoharan, H. C., Lutz, C. P., and Eigler, D. M. (2000). Quantum mirages formed by coherent projection of electronic structure. *Nature*, 403:512–515.

[60] Max-Planck-Gesellschaft, München (2012). Precision Laboratory. Online; accessed 9-October-2017.

[61] Melitz, W., Shen, J., Kummel, A. C., and Lee, S. (2011). Kelvin probe force microscopy and its application. *Surface Science Reports*, 66:1–27.

[62] Morita, S., Wiesendanger, R., and Meyer, E. (2002). *Noncontact Atomic Force Microscopy*. Springer, Berlin, Heidelberg.

[63] Muenks, M. (2017). *Scanning Tunneling Microscopy and Atomic Force Microscopy Measurements on Correlated Systems*. PhD thesis, Universität Konstanz, Konstanz.

[64] Muenks, M., Jacobson, P., Ternes, M., and Kern, K. (2017). Correlation-driven transport asymmetries through coupled spins in a tunnel junction. *Nat Commun*, 8:14119.

[65] Mysliveček, J., Stróżecka, A., Steffl, J., Sobotík, P., Ošt'ádal, I., and Voigtländer, B. (2006). Structure of the adatom electron band of the $\mathrm{Si}(111)-7\times 7$ surface. *Phys. Rev. B*, 73:161302.

[66] Nonnenmacher, M., O'Boyle, M. P., and Wickramasinghe, H. K. (1991). Kelvin probe force microscopy. *Applied Physics Letters*, 58(25):2921–2923.

[67] Oberg, J. C., Calvo, M. R., Delgado, F., Moro-Lagares, M., Serrate, D., Jacob, D., Fernández-Rossier, J., and Hirjibehedin, C. F. (2014). Control of single-spin magnetic anisotropy by exchange coupling. *Nat Nanotechnol*, 9(1):64–8.

[68] Otte, A. F., Ternes, M., von Bergmann, K., Loth, S., Brune, H., Lutz, C. P., Hirjibehedin, C. F., and Heinrich, A. J. (2008). The role of magnetic anisotropy in the kondo effect. *Nat Phys*, 4(11):847–850.

[69] Pan, S. H., Hudson, E. W., and Davis, J. C. (1999). 3he refrigerator based very low temperature scanning tunneling microscope. *Review of Scientific Instruments*, 70(2):1459–1463.

[70] Park, J., Pasupathy, A. N., Goldsmith, J. I., Chang, C., Yaish, Y., Petta, J. R., Rinkoski, M., Sethna, J. P., Abruña, H. D., McEuen, P. L., and Ralph, D. C. (2002). Coulomb blockade and the Kondo effect in single-atom transistors. *Nature*, 417:722–725.

[71] Park, J.-Y., Ham, U. D., Kahng, S.-J., Kuk, Y., Miyake, K., Hata, K., and Shigekawa, H. (2000). Modification of surface-state dispersion upon xe adsorption: A scanning tunneling microscope study. *Phys. Rev. B*, 62:R16341–R16344.

[72] Pascual, J. I., Lorente, N., Grütter, P., Hofer, W., and Rosei, F. (2006). *Single Molecule Vibrational Spectroscopy and Chemistry in "Properties of single organic molecules on crystal surfaces"*. Imperical College Press.

[73] Ploigt, H. C. (2007). *Ultra-Thin Dielectric Layers on Metal Substrates Studied by Scanning Tunneling Microscopy and Scanning Tunneling Spectroscopy*. PhD thesis, EPFL, Lausanne.

[74] Ploigt, H. C., Brun, C., Pivetta, M., Patthey, F., and Schneider, W.-D. (2007). Local work function changes determined by field emission resonances: NaCl/Ag(100). *Phys. Rev. B*, 76(19):195404.

[75] Reinert, F., Nicolay, G., Schmidt, S., Ehm, D., and Hüfner, S. (2001). Direct measurements of the l-gap surface states on the (111) face of noble metals by photoelectron spectroscopy. *Phys. Rev. B*, 63:115415.

[76] Repp, J., Meyer, G., Paavilainen, S., Olsson, F. E., and Persson, M. (2006). Imaging bond formation between a gold atom and pentacene on an insulating surface. *Science*, 312(5777):1196–9.

[77] Repp, J., Meyer, G., and Rieder, K.-H. (2004). Snell's law for surface electrons: Refraction of an electron gas imaged in real space. *Phys. Rev. Lett.*, 92:036803.

[78] Sader, J. E. and Jarvis, S. P. (2004). Accurate formulas for interaction force and energy in frequency modulation force spectroscopy. *Applied Physics Letters*, 84:1801.

[79] Schlegel, R., Hänke, T., Baumann, D., Kaiser, M., Nag, P. K., Voigtländer, R., Lindackers, D., Büchner, B., and Hess, C. (2014). Design and properties of a cryogenic dip-stick scanning tunneling microscope with capacitive coarse approach control. *Review of Scientific Instruments*, 85(1):013706.

[80] Schouteden, K. and Van Haesendonck, C. (2012). Lateral quantization of two-dimensional electron states by embedded ag nanocrystals. *Phys. Rev. Lett.*, 108:076806.

[81] Schwarz, M., Riss, A., Garnica, M., Ducke, J., Deimel, P. S., Duncan, D. A., Thakur, P. K., Lee, T. L., Seitsonen, A. P., Barth, J. V., Allegretti, F., and Auwärter, W. (2017). Corrugation in the weakly interacting hexagonal-bn/cu(111) system: Structure determination by combining noncontact atomic force microscopy and x-ray standing waves. *ACS Nano*, 11(9):9151–9161.

[82] Selloni, A., Carnevali, P., Tosatti, E., and Chen, C. D. (1985). Voltage-dependent scanning-tunneling microscopy of a crystal surface: Graphite. *Phys. Rev. B*, 31:2602–2605.

[83] Smit, R. H. M., Noat, Y., Untiedt, C., Lang, N. D., van Hemert, M. C., and van Ruitenbeek, J. M. (2002). Measurement of the conductance of a hydrogen molecule. *Nature*, 419:906–909.

[84] Stepanow, S., Mugarza, A., Ceballos, G., Gambardella, P., Aldazabal, I., Borisov, A. G., and Arnau, A. (2011). Localization, splitting, and mixing of field emission resonances induced by alkali metal clusters on cu(100). *Phys. Rev. B*, 83:115101.

[85] Steudel, U., Ast, C. R., Motz, U. (2015). Development of low-vibrational foundations for 11 test environments in a newly built precision laboratory. Online; accessed 9-October-2017.

[86] Stipe, B. C., Rezaei, M. A., and Ho, W. (1998). Single-molecule vibrational spectroscopy and microscopy. *Science*, 280(5370):1732–5.

[87] Stradi, D., Barja, S., Díaz, C., Garnica, M., Borca, B., Hinarejos, J. J., Sánchez-Portal, D., Alcamí, M., Arnau, A., Vázquez de Parga, A. L., Miranda, R., and Martín, F. (2012). Electron localization in epitaxial graphene on ru(0001) determined by moiré corrugation. *Phys. Rev. B*, 85:121404.

[88] Stroscio, J. A. and Eigler, D. M. (1991). Atomic and molecular manipulation with the scanning tunneling microscope. *Science*, 254(5036):1319–26.

[89] Stroscio, J. A., Feenstra, R. M., and Fein, A. P. (1986). Electronic structure of the si(111)2 × 1 surface by scanning-tunneling microscopy. *Phys. Rev. Lett.*, 57:2579–2582.

[90] Subramaniam, D., Libisch, F., Li, Y., Pauly, C., Geringer, V., Reiter, R., Mashoff, T., Liebmann, M., Burgdörfer, J., Busse, C., Michely, T., Mazzarello, R., Pratzer, M., and Morgenstern, M. (2012). Wave-function mapping of graphene quantum dots with soft confinement. *Phys. Rev. Lett.*, 108:046801.

[91] Ternes, M. (2006). *Scanning tunneling spectroscopy at the single atom scale*. PhD thesis, EPFL, Lausanne.

[92] Ternes, M., Heinrich, A. J., and Schneider, W. D. (2009). Spectroscopic manifestations of the kondo effect on single adatoms. *J Phys Condens Matter*, 21(5):053001.

[93] Ternes, M., Lutz, C. P., Hirjibehedin, C. F., Giessibl, F. J., and Heinrich, A. J. (2008). The force needed to move an atom on a surface. *Science*, 319(5866):1066–9.

[94] Tersoff, J. and Hamann, D. R. (1983). Theory and application for the scanning tunneling microscope. *Phys. Rev. Lett.*, 50:1998–2001.

[95] Vitali, L., Levita, G., Ohmann, R., Comisso, A., De Vita, A., and Kern, K. (2010). Portrait of the potential barrier at metal-organic nanocontacts. *Nat Mater*, 9(4):320–323.

[96] Wahl, P., Diekhöner, L., Schneider, M. A., Vitali, L., Wittich, G., and Kern, K. (2004). Kondo Temperature of Magnetic Impurities at Surfaces. *Physical Review Letters*, 93(17):176603.

[97] Wittich, G. (2005). *Scanning Tunneling Microscopy and Spectroscopy at Low Temperatures: Development of a 1 K-Instrument and Local Characterization of Heterogeneous Metal Systems*. PhD thesis, Universität Konstanz, Konstanz.

[98] Wolf, S. A., Awschalom, D. D., Buhrman, R. A., Daughton, J. M., von Molnár, S., Roukes, M. L., Chtchelkanova, A. Y., and Treger, D. M. (2001). Spintronics: a spin-based electronics vision for the future. *Science*, 294(5546):1488–95.

[99] Ye, C., Marks, T. J., Yang, J., and Wong, G. K. (1987). Synthesis of molecular arrays with nonlinear optical properties: second-harmonic generation by covalently functionalized glassy polymers. *Macromolecules*, 20:2322–2324.

[100] Zerweck, U., Loppacher, C., Otto, T., Grafström, S., and Eng, L. M. (2005). Accuracy and resolution limits of kelvin probe force microscopy. *Phys. Rev. B*, 71:125424.